Optimizing a dynamic fossil fuel CO_2 emission model with CTDAS (v1.0) for an urban area using atmospheric observations of CO_2, CO, NO_x, and SO_2

Ingrid Super[1,2], Hugo A.C. Denier van der Gon[1], Michiel K. van der Molen[2], Stijn N.C. Dellaert[1], Wouter Peters[2,3]

[1]Department of Climate, Air and Sustainability, TNO, P.O. Box 80015, 3508 TA Utrecht, Netherlands
[2]Meteorology and Air Quality Group, Wageningen University, P.O. Box 47, 6700 AA Wageningen, Netherlands
[3]Centre for Isotope Research, Energy and Sustainability Research Institute Groningen, University of Groningen, Nijenborgh 4, 9747 AG Groningen, Netherlands

Correspondence to: Ingrid Super (ingrid.super@tno.nl)

1

Abstract. We present a modelling framework for fossil fuel CO_2 emissions in an urban environment, which allows constraints from emission inventories to be combined with atmospheric observations of CO_2 and its co-emitted species CO, NOx, and SO_2. Rather than a static assignment of average emission rates to each unit-area of the urban domain, the fossil fuel emissions we use are dynamic: they vary in time and space in relation to data that describe or approximate the activity within a sector, such as traffic density, power demand, 2m temperature (as proxy for heating demand), and sunlight and wind speed (as proxies for renewable energy supply). Through inverse modelling, we optimize the relationships between these activity data and the resulting emissions of all species within the dynamic fossil fuel emission model, based on atmospheric mole fraction observations. The advantage of this novel approach is that the optimized parameters (emission factors and emission ratios, N=44) in this dynamic emission model (a) vary much less over space and time, (b) allow a physical interpretation of mean and uncertainty, and (c) have better defined uncertainties and covariance structure. This makes them more suited to extrapolate, optimize, and interpret than the gridded emissions themselves. The merits of this approach are investigated using a pseudo-observation-based ensemble Kalman filter inversion setup for the Dutch Rijnmond area at 1x1 km resolution.

We find that the fossil fuel emission model approximates the gridded emissions well (annual mean differences < 2 %, hourly temporal r2 = 0.21–0.95), while reported errors on the underlying parameters allow a full covariance structure to be created readily. Propagating this error structure into atmospheric mole fractions shows a strong dominance of a few large sectors and a few dominant uncertainties, most notably the emission ratios of the various gases considered. If these are either sufficiently well-known a-priori, or well-constrained from a dense observation network, we find that including observations of co-emitted species improves our ability to estimate emissions per sector relative to using CO_2 mole fractions only. Nevertheless, the total CO_2 emissions can be well-constrained with CO_2 as only tracer in the inversion. Because some sectors are sampled only sparsely over a day, we find that propagating solutions from day-to-day leads to largest uncertainty reduction and smallest CO_2 residuals over the 14 consecutive days considered. Although we can technically estimate the temporal distribution of some emission categories like shipping separate from their total magnitude, the controlling parameters are difficult to distinguish. Overall, we conclude that our new system looks promising for application in verification studies, provided that reliable urban atmospheric transport fields and reasonable a-priori emission ratios for CO_2 and its co-emitted species can be produced.

2

1 Introduction

Within the 2015 Paris Agreement, 195 nations agreed with a climate action plan in which each nation sets its own targets for carbon emission reductions and reports all efforts regularly to the UNFCCC (UNFCCC, 2015). An important role in reaching emission reduction targets is laid out for cities, which emit a large portion of the global fossil fuel CO_2 emissions (about 70 % according to the International Energy Agency (IEA, 2008)). The Paris Agreement also states that parties should strengthen their cooperation, also with respect to the sharing of information and good practices. Within this context it becomes increasingly important to map fossil fuel emissions and to quantify emission trends, both at the country- and city-level.

Most country-level greenhouse gas emission estimates reported to the UNFCCC are currently based on annual fuel consumption data (bottom-up method), and are often spatiotemporally disaggregated using activity data and proxies to create spatially explicit emission inventories (Kuenen et al., 2014; Hutchins et al., 2017). Although the annual national estimates are reasonably accurate (estimated uncertainty for developed countries is less than 8 % for CO_2 (Monni et al., 2004; Fauser et al., 2011; Andres et al., 2014)), their uncertainty increases rapidly when disaggregating them towards finer spatiotemporal resolutions (Ciais et al., 2010; Nassar et al., 2013; Andres et al., 2016). A method to improve emission estimates is using transport models in combination with independent observations of atmospheric mole fractions (Palmer et al., 2018), called data assimilation (DA) or inverse modelling (a top-down method). Recently, efforts have been made to apply DA techniques to the urban environment (McKain et al., 2012; Brioude et al., 2013; Lauvaux et al., 2013; Bréon et al., 2015; Boon et al., 2016; Lauvaux et al., 2016; Staufer et al., 2016; Brophy et al., 2018), but several challenges and unexploited opportunities remain.

First, urban DA studies have tried to constrain the total fossil fuel flux to validate bottom-up CO_2 inventories, often without considering the underlying emission process that caused the mismatch between observed and modelled concentrations. As one of very few exceptions, Lauvaux et al. (2013) used the $CO:CO_2$ concentration ratio to conclude that the emission reduction in Davos during the World Economic Forum 2012 was likely related to reduced traffic emissions, but without a quantification. However, emission reduction policies usually target specific source sectors. Therefore, an increase in fossil fuel emissions from one source sector can cause the total CO_2 emissions to appear stable, although a policy targeting another source sector can be effective in itself. To monitor the effect of each measure independently it becomes essential to attribute changes in the total CO_2 emissions to these policies and thus to specific source sectors. It is, therefore, not sufficient to constrain the total CO_2 flux, but we need to differentiate the total CO_2 signal into signals from the different source sectors. One way to accomplish this is by using additional measurements of co-emitted species and isotopes. Such measurements have previously been used in modelling studies to differentiate between biogenic and anthropogenic emissions or between fuel types (Djuricin et al., 2010; LaFranchi et al., 2013; Lopez et al., 2013; Turnbull et al., 2015; Fischer et al., 2017; Super et al., 2017b; Brophy et al., 2018; Graven et al., 2018), but also to separate between different fossil fuel sources (Lindenmaier et al., 2014; Super et al., 2017a; Nathan et al., 2018).

Second, for urban DA the fine scales (less than 1km and less than 1 hour) need to be resolved, therefore putting a higher demand on the atmospheric transport models. For example, Boon et al. (2016) mentioned that sources with a small spatial extent (point sources) are not correctly represented on a 2x2 km^2 grid, while these sources have a significant impact on the locally observed mole fractions. Concurrently, we have previously shown that a plume model improves the representation of sources with a limited spatial extent. Moreover, we found that the description

3

79 of short-term variations in the wind direction by the Eulerian WRF model in the vicinity of an urban area is poor
80 (Super et al., 2017a).

81 Third, the prior emissions also need to have a higher resolution for urban-scale studies to resolve the dominant
82 spatiotemporal variations. Previous studies have often used high-resolution emission maps developed specifically
83 for that region, using local data as much as possible (Zhou and Gurney, 2011; Bréon et al., 2015; Boon et al., 2016;
84 Lauvaux et al., 2016; Rao et al., 2017; Gurney et al., 2019). Yet such emission maps are only available for a few
85 data-rich regions. For other regions, continental or global emission maps (such as MACC or EDGAR) can be used
86 if downscaling is applied to reach the high resolution required for urban-scale inversions. For example, the
87 temporal downscaling can be done using typical daily, weekly and monthly profiles for each source sector (Denier
88 van der Gon et al., 2011), which are based on activity data (e.g. traffic counts) averaged over several years and/or
89 a large region. Spatial downscaling often involves proxies like population density. This spatiotemporal
90 downscaling introduces a large additional uncertainty due to uncertainties in the proxies. For example, Hogue et
91 al. (2016) have found an uncertainty of 150 % in the 1x1 ° fossil fuel CO_2 emissions for the US, whereas Ciais et
92 al. (2010) estimated the uncertainty of regional European emissions at 100 km resolution to be about 50 %.
93 Quantification of the uncertainty at an even higher resolution for urban applications has so far been limited (Andres
94 et al., 2016; Super et al., 2020), also for most local inventories, while a correct definition of the prior error
95 covariance matrix for an inversion is important to get reliable output (Chevallier et al., 2006; Boschetti et al.,
96 2018). This currently complicates the application of DA studies to urban areas.

97 Here, we describe the development of an urban-scale DA framework (based on the CarbonTracker Data
98 Assimilation Shell (CTDAS) (Van der Laan-Luijkx et al., 2017)) which uses a dynamic fossil fuel emission model
99 as a prior and optimizes the parameters of this model. The fossil fuel emission model uses a wide range of
100 (statistical) data to calculate CO_2 emissions per source sector at high spatiotemporal resolution (1x1 km2 and
101 hourly). The emission model is more dynamic than a regular emission inventory in the sense that its formulation
102 allows emissions to change as a function of rapidly varying conditions in the emission landscape, such as the
103 outside temperature, the traffic density, or availability of wind and solar radiation for sustainable power generation.
104 Using such information enables the calculation of dynamic emissions without a two-year lag, as opposed to the
105 construction of a static emission map based on statistical downscaling. Moreover, the emission model can supply
106 spatiotemporal emission uncertainties and error correlations between source sectors, based on the estimated
107 uncertainty of its model parameters. Since many of these parameters are also used in bottom-up accounting of
108 emissions, their uncertainty is often better established than the uncertainty in the total emissions themselves.
109 Finally, we use the emission model to calculate emissions of other co-emitted species (CO, NO_x and SO_2) from
110 the CO_2 emissions using source sector specific emission ratios. These co-emitted species are included in the DA
111 system to facilitate source attribution, which is possible due to the distinct emission ratios of different source
112 sectors. The overall aim of this study is to explore how our fossil fuel emission model and additional tracers can
113 be used to overcome the known limitations in anthropogenic CO_2 inverse modelling described above. The research
114 questions are:

1. Can our dynamic fossil fuel emission model represent the spatiotemporal structure of a high-resolution
    emission inventory, and what does it add to that on small scales?
2. Is the addition of co-emitted species beneficial for the attribution of CO_2 signals to specific source sectors,
    and which observations help most in that effort?

4

3. Does the prior error covariance structure that we build with the dynamic emissions model help the optimization, and what can we learn from the posterior error covariance estimate?

In the inverse modelling part of this study we use observing system simulation experiments (OSSEs, experiments using pseudo-observations), applied to the urban-industrial complex of Rotterdam (Netherlands). This choice allows us to test our new approach, while with real observations the errors in non-fossil and background fluxes, model structure, and model transport will likely dominate the results (Tolk et al., 2008; Super et al., 2017a; He et al., 2018) and reduce the ability to evaluate the methodology. First, we give an overview of the dynamic fossil fuel emission model and demonstrate its applicability to the domain, followed by an introduction to the DA system components and the model settings. Then we discuss the different experiments in which we start with the comparison of different network configurations, one with only CO_2 and one including co-emitted species to examine the ability to attribute CO_2 emissions to specific source sectors, and different state vectors. Another experiment is used to examine the importance of propagating posterior parameters values and covariances. Finally, we address the effect of cross-correlations.

2 Methods

2.1 The dynamic emission model
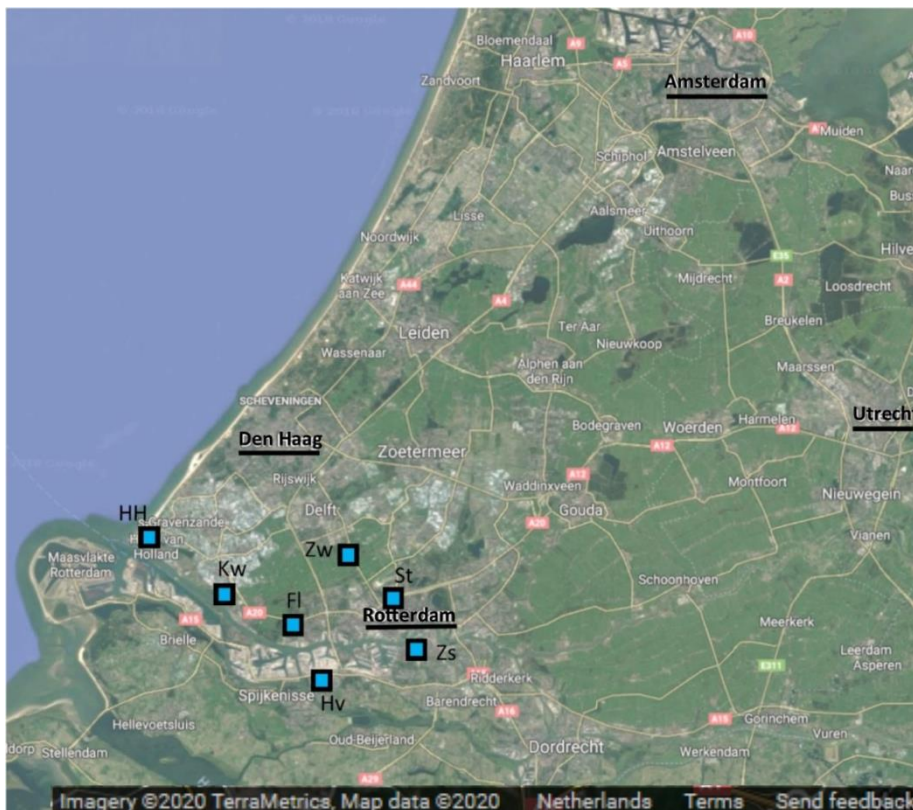
Figure 1. Map of the domain covered (Randstad area, the Netherlands) within this study, including major cities Amsterdam, Rotterdam, The Hague, and Utrecht (underlined). The squares show the locations of the measurement sites within the urban network configuration. The area of this domain is approximately 77x88 km. Source: ©Google Maps.

Although generally applicable, the dynamic emission model is initially developed for the Netherlands and focused on Rotterdam (Fig. 1). This is one of the major cities in the Netherlands (about 625,000 inhabitants) with the largest sea port of Europe to its west. It is located in a larger urbanized area (Randstad, about 7 million inhabitants)

5

with The Hague, Amsterdam and Utrecht being other major cities. A large area to the southwest of The Hague is used for glasshouse horticulture producing vegetables and flowers. The Rotterdam area is characterized by a complex mixture of residential and industrial activities and therefore we distinguish five source sectors and a total of ten sub-sectors to construct its emissions (see Table 1). Note that, for simplicity, only the largest source sectors are included, which are responsible for >95 % of the CO_2 emissions in the area. Moreover, a further subdivision of industrial activities is neglected because of two reasons: 1) the lack of data for each subsector and 2) the inability to separate between those activities with atmospheric measurements because of their spatial clustering. The main goal is to get a reasonable first estimate of the emission landscape using readily available data.

Table 1. Overview of source sectors and subsectors distinguished in the dynamic emission model, including their short name used in the figures, whether they are represented as point or area sources, and their approximate contribution to the total CO_2 emission in Rotterdam (Netherlands PRTR, 2014). Crosses indicate which emission factors (EF), and tracer ratios of CO, NOx or SO2 (Rco, RNOx, RSO2) are part of the state vector and circles indicate whether they are also part of the short state vector (see Sect. 2.3).

| Source sector	Subsector	Short name	Source type	Contribution	EF	R_{CO}	R_{NOx}	R_{SO2}
Power plants	Gas-fired power plants	1A	Point	37 %	XO	X	X	
	Coal-fired power plants	1B			XO	X	X	X
Non-industrial combustion	Households	2A	Area	15 %	XO	XO	X	X
	Glasshouses	2B			XO	X	X	
Industry		3	Point	39 %	XO	XO	XO	XO
Road traffic	Cars	7A	Area	6 %	XO	XO	XO	
	Heavy duty vehicles	7B			XO	XO	XO	
Shipping	Ocean shipping	8A	Area	3 %	XO	X	XO	XO
	Inland shipping	8B			XO	X	XO	XO
	Recreational shipping	8C						

The ultimate goal is to develop an emission model that assimilates high-resolution activity data, such as traffic data, in near real-time. A truly dynamic emission model is not dependent on pre-calculated annual emissions and spatial or temporal downscaling, but directly uses activity data to calculate emissions for that specific moment. However, the development of a dynamic emission model still requires a lot of research. Here, we make a first step by mainly illustrating the potential of using high-resolution activity data to better represent temporal variations. In this work, the emissions are calculated in four steps. First, the annual, national emission is calculated per sector using reported annual activity data and CO_2 emission factors. Second, we apply temporal disaggregation to hourly emissions using time profiles based on a combination of default temporal profiles, and environmental conditions. Third, we downscale the national totals to 1x1 km^2 resolution using statistical data, such as population density. Finally, our approach also allows uncertainties to be described in detail based on parameters in Eq. (2).

2.1.1 Step 1: Sectorial total emission calculations

167   Total annual emissions (F_X in kg yr^{-1}) per sector and species (X=CO_2, CO, NO_x, SO_2) are calculated as a function

168   of the economic activity and an emission factor (adapted from Raupach et al. (2007)):

169    $$F_X = A\left(\frac{E}{A}\right)\left(\frac{F_{CO2}}{E}\right)R_X \hspace{4cm} (1)$$

170   where A is the amount of activity (which often has the unit € when GDP or industrial productivity is used as proxy)

171   and E is the primary energy consumption (petajoule (PJ)). R_X is the emission ratio needed to calculate emissions

172   of co-emitted species X from the CO_2 emissions (kg kg^{-1}), which is specific for each economic sector (R_{CO_2} is

173   always 1, others are illustrated in Fig. 2). In this equation the term F_{CO2}/E is the CO_2 emission factor (EF), i.e. the

174   amount of CO_2 emitted per amount of energy consumed. The term E/A can be seen as a measure of energy

175   efficiency, in which technological development plays an important role (Nakicenovic et al., 2000).
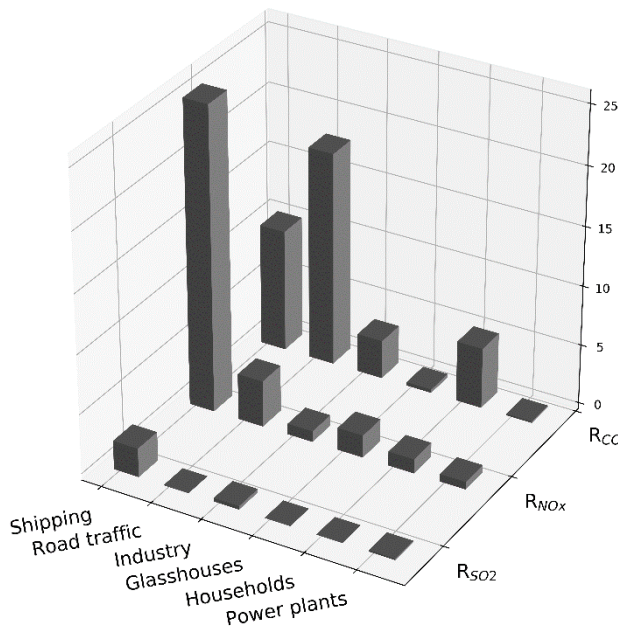
176
177   **Figure 2. Emission ratios of CO:CO_2 (R_{CO}), NO_x:CO_2 (R_{NOx}) and SO_2:CO_2 (R_{SO2}) for specific source sectors based on**
178   **the Dutch Pollution Release and Transfer Register (Netherlands PRTR, 2014). Units are in ppb ppm^{-1}. A value of 10 on**
179   **the y-axis thus implies that for each 1000 moles of CO_2, 10 moles of the auxiliary tracer is emitted.**

180   The information needed in Eq. (1) comes from various inventories and national information sources. For example,

181   changes in annual activity can be approximated based on national statistics such as the GDP (Gross Domestic

182   Product), which can be a proxy for industrial activity. Or A can be based on environmental data such as the annual

183   degree day sum based on the outside temperature, as proxy for the need for household heating in a particular year.

184   These proxies for A are known globally, which is why we use Eq. (1) instead of directly using energy consumption

185   data (E). For local studies more specific activity data could be used, for example vehicle kilometres driven as a

186   predictor for road traffic emissions. The second term in Eq. (1) (E/A, the energy efficiency) can be estimated from

187   activity data and energy consumption statistics, such as available from the International Energy Agency or data

188   from national statistics agencies. Even if E is not directly available for a country, an estimate can be made based

189   on a country with a comparable level of development and climatology. Note that this term can show a large trend

190   in case of technological development. The last terms in Eq. (1) (F/E and R_x, the emission factors) are the most

191   uncertain ones, because the emission factor is dependent on the fuel mix and the energy efficiency, which itself

192   can vary with environmental conditions (e.g. a cold engine on a winter day burns less efficiently). It can therefore

193   differ significantly between countries. Emission factor values that are generally valid can be gathered from the

7

194   Intergovernmental Panel on Climate Change (IPCC) or the European Environmental Agency (EEA), while

195   country-specific values are typically less easily accessible. For our study area, we have access to both EEA data,

196   as well as to Netherlands-specific numbers and even to Rijnmond-specific values (Netherlands PRTR, 2014) . See

197   Appendix A for a full overview of the data used.

2.1.2 Step 2: Temporal profiles and parameterizing activity

199   The second step is to disaggregate the annual emissions to hourly emissions by calculating time profiles, such that

200   Eq. (1) becomes "dynamic":

201    $$F_{X,t} = A \left(\frac{E}{A}\right) \left(\frac{F_{CO2,t}}{E}\right) R_X T_t \tag{2}$$

202   where T_t is the hourly time factor and F is in kg h^{-1} (hence the subscript t). Averaged over a year the value of T_t is

203   1.0, so that it only alters the temporal evolution and not the total emissions. Energy use is often specifically linked

204   to an activity (A in Eq. (1) and Eq. (2)) on which temporal information is more readily available than on the

205   resulting emissions. Therefore, T_t can be calculated in two ways: 1) by directly using temporally explicit activity

206   data or 2) by parameterizing temporal variations from environmental and/or economic conditions. When activity

207   data is available the first option is preferable. However, in data-sparse regions the second option might be

208   necessary to implement, which is still an improvement compared to long-term average profiles as commonly used

209   as we will discuss next for several sectors represented in our emission model. Appendix B provides an overview

210   of the data that is used per sector.

211   Non-industrial combustion is dominated by households' natural gas consumption to heat houses, for cooking, and

212   for warm water supply. A Dutch energy provider has a dataset publicly available from about 80 smart meters for

213   the year 2013 with hourly gas consumption (Liander, 2018). It clearly shows a seasonal cycle, but also more small-

214   term variations (daily data are shown in Fig. 3). We also see higher gas consumption in the beginning of the year,

215   where the first three months of 2013 had some long, cold spells.

216   The use of energy for household heating is connected to the outside temperature. Previous studies have therefore

217   used the concept of heating degree days to describe the temporal variability in emissions from households (Mues

218   et al., 2014; Terrenoire et al., 2015). This method weighs all daily mean temperatures below a certain temperature

219   threshold (here 18°C, as suggested by Mues et al. (2014)) and assigns emissions to these days accordingly. Besides

220   heating, gas consumption is related to warm water supply and cooking, which is largely independent of the outside

221   temperature. Therefore, a constant offset is assumed of 20%, similar to Mues et al. (2014). More details can be

222   found in Appendix B.

223   We compared the heating degree day method using observed temperature data from the Royal Netherlands

224   Meteorological Institute (KNMI) with gas consumption data on a daily basis (Fig. 3). The degree day function

225   follows the gas consumption data very well, including the higher consumption at the start of the year, reaching an

226   R^2 of 0.90 (N=365). The gas consumption of consumers also has a diurnal pattern with peaks in the early morning

227   and late afternoon. Therefore, a diurnal profile can be estimated based on typical working hours, for which we

228   used profiles from Denier van der Gon et al. (2011). For hourly data R^2 is 0.80 (N=8760, not shown).

8
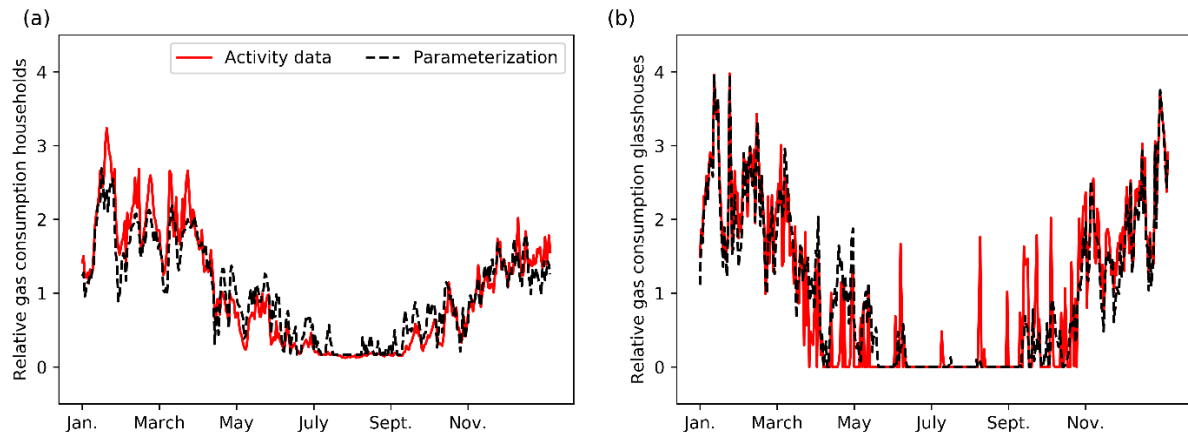
Figure 3. Daily time profiles for households (a) and glasshouses (b). Solid red lines are based on true activity data, whereas dashed black lines are parameterizations based on the degree day function.

For the energy consumption of glasshouses there is no true activity data available. Instead, we use modelled daily energy consumption for a typical Dutch glasshouse cultivating tomatoes (courtesy of Bas Knoll, TNO) as the 'truth' (activity data). This time profile is calculated for typical meteorological conditions, such that the order of magnitude and the peaks are representative for an average year. There is almost no energy consumption during the summer, which indicates that there is no constant offset. So, we use the heating degree day function with no constant offset to determine the time factors. Moreover, we use a lower temperature threshold of 15 °C to get a better fit with the observed energy consumption. During summer several days show a peak in the relative gas consumption, suggesting that the average temperature has dropped below the threshold. The estimated function compares well with the activity data (Fig. 3) with an R^2 of 0.85 (N=365). The diurnal cycle of glasshouse emissions is likely to be different from that of household emissions. Yet we lack data to establish a diurnal cycle. We therefore use the same diurnal profile as for households, although this is likely to be incorrect.

Power plants can use different fuels such as hard coal, natural gas or biomass. In the Netherlands coal-fired and gas-fired power plants account for 80–85 % of the total energy production. The remainder comes mainly from wind energy (5–6 %) and biomass burning (5–6 %). Power generation data are reported by the European Network of Transmission System Operators for Electricity (ENTSO-E), which has detailed data available for the whole of Europe (Hirth et al., 2018). Coal-fired power plants are currently the main source of energy and their generation is relatively stable compared to other sources. It does, however, show a seasonal cycle with less energy production during the summer months. Gas-fired power plants have a larger temporal variability as they are mainly used as back-up for peak hours, depending also on the amount of renewable energy that is available.

We use the degree day function to estimate the time profiles of both coal- and gas-fired power plants. Linear regression analysis shows that the coal-fired power generation is correlated with degree days ($R^2 = 0.17$). In this case we use a large constant offset of 80 % and a threshold of 25 °C which were chosen to best match the actual power generation data. The offset is much larger than for households because there is always a basic energy demand from the industry. In contrast, the gas-fired power plants are (negatively) correlated with the wind speed ($R^2 = 0.13$) and incoming solar radiation ($R^2 = 0.10$), which may indicate a higher need for gas-fired power generation in the absence of renewable sources. Therefore, we replace the temperature in the degree day function with the multiplication of wind speed (threshold of 10 m s^{-1}) and incoming solar radiation (threshold of 150 J cm^{-2}). A constant offset of 10 % is assumed.

9

260 The diurnal cycles for power plants can be based on socio-economic factors. For example, the energy demand
261 peaks early in the morning when people get ready to go to work and at the end of the afternoon when they get
262 home. We find this pattern in the actual power generation data, with coal-fired power plants being less variable
263 during the day than gas-fired power plants. The fixed profile from the European MACC-III emission inventory
264 (Denier van der Gon et al., 2011; Kuenen et al., 2014) matches reasonably well with gas-fired power plant profiles,
265 but it is less applicable for coal-fired power plants (Fig. 4). Overall, the estimated profiles for gas-fired power
266 plants (daily/hourly data) have an R^2 of 0.31/0.32 (N=366/8784) when compared to the activity data. For coal-
267 fired power plants this is 0.17/0.21 (N=366/8784).

268 The constant offset of 80% for coal-fired power plants is mainly caused by the energy demand of the industry and
269 other semi-continuous processes. Taking into account seasonal variations in these processes could improve the
270 timing of coal-fired power plant activities, probably increasing the power generation in winter relative to the
271 summer holiday period. Moreover, the renewable energy supply is probably better modelled when taking into
272 account a larger domain, since the energy supply is not just local. With a better prediction of the amount of
273 renewables we could improve the timing of the gas-fired power plant emissions, which mostly function as a back-
274 up for renewable energy.
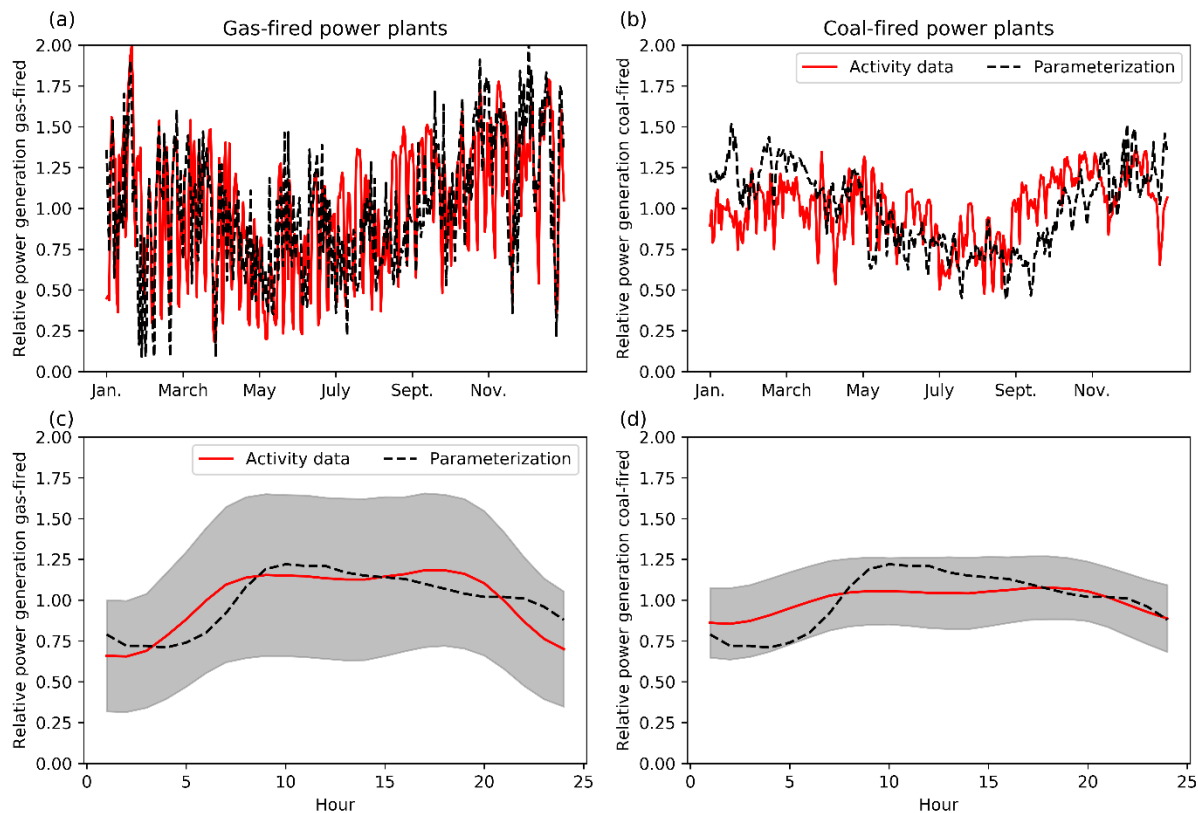
Figure 4. (top row) Daily time profiles for gas-fired (a) and coal-fired (b) power plants. Solid red lines are based on true activity data, whereas dashed black lines are parameterizations based on observed temperature (coal) and wind speed/radiation (gas). (bottom row) Average diurnal cycle for gas-fired (c) and coal-fired (d) power plants. Solid red lines are based on true activity data, whereas dashed black lines are fixed profiles from the MACC inventory (Denier van der Gon et al., 2011; Kuenen et al., 2014). Shading gives the 1σ variability of the diurnal cycle based on activity data.

282 The industrial sector consists of a wide range of activities, of which some are semi-continuous and only interrupted
283 by maintenance stops while others follow working hours. This makes it very difficult to predict the temporal
284 variability, especially for the overall sector. Since the largest CO_2 emissions are related to refineries and heavy

10

industry we will focus on these activities. We find a seasonal cycle in the reported industrial activity, with a small decline during the summer and Christmas holidays. However, the variations are very small (max. 1 %). Therefore, we assume constant emissions.

Road transport emissions can vary between different road and vehicle types (Mues et al., 2014), but are also strongly dependent on environmental, socio-economic and driving conditions (such as the amount of stops, free-flow versus stagnant conditions, and engine temperature). Traffic count data are often used to create average time profiles for road traffic emissions, although with traffic counts we are unable to account for environmental and driving conditions. Traffic counts for the Netherlands are made available by the Nationale Databank Wegverkeersgegevens (NDW) and similar data is available in many developed countries. We differentiate between two vehicle types (passenger cars + motorcycles (hereafter referred to as cars) and light duty + heavy duty vehicles (hereafter referred to as HDV)) and three road types (highway, main road, urban road). We selected all available locations for 2014 within or close to Rotterdam that distinguish 3-5 vehicle lengths and filtered for a minimum data coverage of 75 %. This leaves us with 25 highway, 6 main road and 13 urban road locations. From this data we make average time profiles (daily, weekly and monthly) per road and vehicle type, as is often done to disaggregate road traffic emissions. Note that this method excludes any spatial variations (e.g. highways leading towards the city vs. the beach), except for differentiating between road types.

Generally, HDV show a larger spread due to the low counts during the weekend (Fig. 5). Car counts on weekdays show a morning and evening rush hour and they go down in between. In contrast, HDV counts peak throughout the day and only go down after the evening rush hour. Moreover, the diurnal cycles are different during the weekend than on weekdays. These patterns can be explained from socio-economic factors. Current time profiles are often based on cars and are unable to correctly represent the temporal variability of HDV. This also affects the spatial distribution of emissions and therefore we create average diurnal, weekly and seasonal profiles separately for cars and HDV, for different road types and considering the day of the week. The comparison of true traffic counts and averaged traffic counts results in R^2 values between 0.83 and 0.95 for hourly data for the whole year (N between 2665 and 6471 because of gaps in the traffic count data).
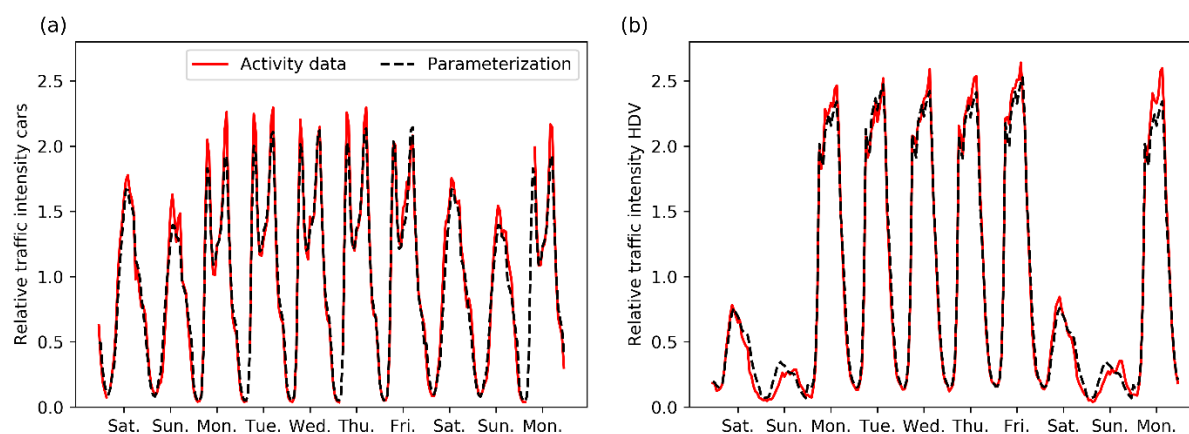
Figure 5. Time profiles of passenger cars (a) and heavy-duty vehicles (b) road transport on highways for ten randomly chosen days in March. Solid red lines are based on true activity data, whereas dashed black lines are parameterizations based on averaged traffic counts for Rotterdam.

Shipping emissions are dependent on the type of fuel used and whether ships apply slow-steaming. Additionally, during loading and unloading ships still emit CO_2 and other pollutants, even though they are not moving. Such information is currently not available, so instead we use information about the arrival and departure of ships in the

11

port of Rotterdam to make a time series of ship movements. Note that this only applies to large vessels that transport goods and passengers and that the time profile will look different for recreational shipping. However, large ships account for approximately 80 % of the total shipping emissions in the area of interest. Since we lack information about other type of shipping movements, we will only account for large ships in the time profiles.

We collected ship movements for one month (daily data) and an average diurnal profile. The diurnal cycle shows a peak throughout the day, which corresponds well with the HDV road transport emission patterns on highways. The reason for this is that HDV road transport is related to shipping movements, as HDV takes care of part of the good transport further inland after the goods have arrived by ship. We also find a clear weekly pattern with less ship movements during the weekend, although the decrease is less than for HDV road transport. This is likely because large ships, such as entering the port of Rotterdam, continue travelling during the weekend. Therefore, the weekly pattern resembles more that of car road transport on highways. Thus, we can estimate ship movements by using the temporal profiles of HDV and cars on highways. This method is specifically tested for Rotterdam and different patterns might be visible elsewhere. We also use HDV patterns for the seasonal variability, and final parameterized and reported activity in this method reach an R^2 value of 0.89 for a period of 18 days with hourly data (N=432) as shown in Fig 6.
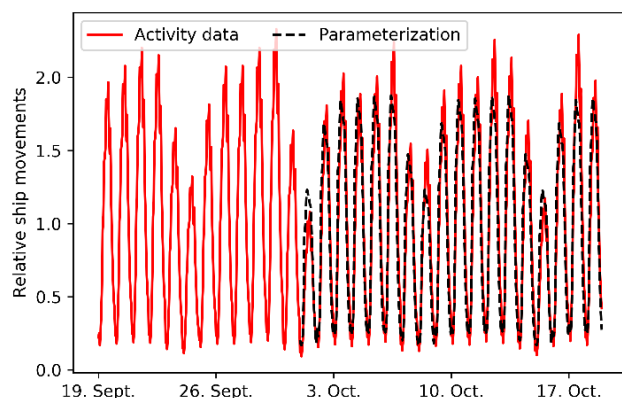
Figure 6. Daily time profiles for shipping. Solid red line is based on true activity data, whereas dashed black line is a parameterization based on traffic counts of heavy-duty vehicles (diurnal cycle) and cars (day-to-day variations) on highways.

2.1.3 Step 3: Spatial disaggregation.

National total sectorial emissions need to be distributed into spatially explicit emissions for our study domain. The spatial disaggregation of emissions has already received attention from inventory builders. Existing emission inventories can be used to describe the spatial disaggregation, if available for the region at high resolution. Therefore, no extra effort is put in the spatial disaggregation and the spatial patterns from the Dutch Emission Registration have been adopted (Netherlands PRTR, 2014).

In absence of a high-resolution inventory, simple default proxies for the spatial distribution can be used, such as population density (e.g. Gridded Population of the World (GPW)) and the presence of roads or waterways (e.g. OpenStreetMap). Generally, these proxies are also used by inventory builders, but are often updated to take into account local circumstances. For example, main roads and urban roads are busiest in densely populated areas and we can assume emissions on main and urban roads are correlated with population density. Highways are used for transport between cities and therefore emissions take place outside densely populated areas as well. Nevertheless, highway transport is usually to and from densely populated areas, such that most emissions will take place close to cities. We can therefore relate these emissions with the population density in the area of interest (in this case

12

Rijnmond) relative to the rest of the country, which places the same amount of the country-level emissions in our case study domain as the gridded inventory. Additionally, the location of large power plants or industrial plants is often known (for example from E-PRTR (Pollutant Release and Transfer Register)), which can be used directly. Although such information allows us to possibly construct a detailed fossil fuel model in data-sparse regions in the future, in this study we focus first on the more easily implementable and less-developed parameterization of temporal activity in different sectors (step 2) to assess whether this approach is promising enough for future extension.

2.1.4 Step 4: Uncertainty analysis

The emission model we have constructed in steps 1–3 contains several parameters per source sector: activity, emission factor, spatial proxy and time profile. For the analysis we only consider the emission factors and time profiles, as we assume activity data and the spatial distribution to be (a) well-known for our study area, and (b) mostly unobservable from the network of only 7 sites which is used here to evaluate our approach (see Sect. 2.2.3). Although the spatial distribution is actually a large source of uncertainty, we aim at optimizing parameter values that are valid for the entire case study area and for simplicity we ignore the spatially variable uncertainties. Nevertheless, it is possible to incorporate spatial uncertainties in this methodology as well, as illustrated by Super et al. (2020).

As input for step 1 in the dynamic emission model we use generalized parameters which we take from the IPCC, EEA and other organizations. These databases also provide an uncertainty range, which we use in a final step to create a covariance matrix. The covariance matrix describes the Gaussian uncertainty of these parameters (diagonal values) and error correlations between parameters (off-diagonal values). From the covariance matrix we create an ensemble of parameters (N=500) that represents their joint distributions, and we use them to calculate an ensemble of emissions. In this Monte Carlo simulation, we transform some Gaussian parameters into log-normal distributions to account for non-negativity, or to account for distributions with a very long tail (mainly emission ratios, which can become high in specific cases where no emission reduction measures are taken). Appendix A summarizes the used parameter values and uncertainties (including the shape of the distributions) and shows an example of the covariance matrix. This method is a first step towards a better quantification of parameter uncertainties and error correlations and additional effort has already been made to improve this method (Super et al., 2020).

In a final step, we select the most important parameters which are either very uncertain or have a large impact on the total emissions. This leaves us with the 44 parameters that we optimize in a set of data assimilation experiments, described next. In Sect. 3.1 we report uncertainties in % (1 σ) for normal distributions (CO_2) or as a 90 % confidence interval (CI) for lognormal distribution (co-emitted species).

2.2 Data assimilation to estimate fossil fuel sources

The goal of data assimilation is to find a state at which the system is in optimal agreement with observations. In this work, the observations we want to explore are the mole fractions of CO_2 and its co-emitted species while the state of the system is the underlying spatiotemporal distribution of fossil fuel emissions. Such configurations are sometimes referred to as "FFDAS" (fossil fuel data assimilation systems) applications, with a number of examples in recent literature (Rayner et al., 2010; Asefi-Najafabady et al., 2014; Basu et al., 2016; Graven et al., 2018).

13

388   Given the sparsity of approaches explored so far, the dynamic emission model with its parameter driven emissions
389   we present here could lend itself well for application in an FFDAS, and this is what we explore through a set of
390   experiments with our own data assimilation methodology.

391   In this study we use the CarbonTracker Data Assimilation Shell (CTDAS) (v1.0) described in detail in Van der
392   Laan-Luijkx et al. (2017). Briefly, the CTDAS system is a flexible implementation of a square-root Ensemble
393   Kalman Filter (Whitaker and Hamill, 2002), which also allows lagged windows (i.e. smoothing instead of
394   filtering). The Ensemble Kalman Filter optimizes the cost function for unknown variables in the state vector x
395   using information from observations ($\mathbf{y}^0$ with covariance $\mathbf{R}$) and a prior estimate of the state vector ($\mathbf{x}^b$ with
396   covariance $\mathbf{P}$).

397    $$J(\mathbf{x}) = \left(\mathbf{y}^0 - \mathcal{H}(\mathbf{x})\right)^T \mathbf{R}^{-1}\left(\mathbf{y}^0 - \mathcal{H}(\mathbf{x})\right) + \left(\mathbf{x} - \mathbf{x}^b\right)^T \mathbf{P}^{-1}\left(\mathbf{x} - \mathbf{x}^b\right) \tag{7}$$

398   In this function, $\mathcal{H}$ is the observation operator that returns simulated mole fractions given the state vector. $\mathbf{R}$ and
399    $\mathbf{P}$ determine how much weight is given to the observations and prior estimate, respectively.

400   The optimized state vector (indicated with superscript a, whereas b refers to the prior estimates) which minimizes
401   the cost function is

402 $$\mathbf{x}^a = \mathbf{x}_t^b + \mathbf{K}(\mathbf{y}_t^0 - \mathcal{H}(\mathbf{x}_t^b)) \tag{8}$$

403   and its covariance is

404    $$\mathbf{P}_t^a = (\mathbf{I} - \mathbf{KH})\mathbf{P}_t^b \tag{9}$$

405   Here, $\mathbf{H}$ is the linearized observation operator and $\mathbf{K}$ is the Kalman gain matrix:

406    $$\mathbf{K} = \left(\mathbf{P}_t^b \mathbf{H}^T\right)\left(\mathbf{HP}_t^b \mathbf{H}^T + \mathbf{R}\right)^{-1} \tag{10}$$

407   The solutions of Eq. (8) and Eq. (9) are calculated as in Peters et al. (2005) using an ensemble of 80 members. The
408   choice for the ensemble size was based on the typical dimensions of our inverse problem, which has N=1960
409   observations and M=44 unknowns for the base run.
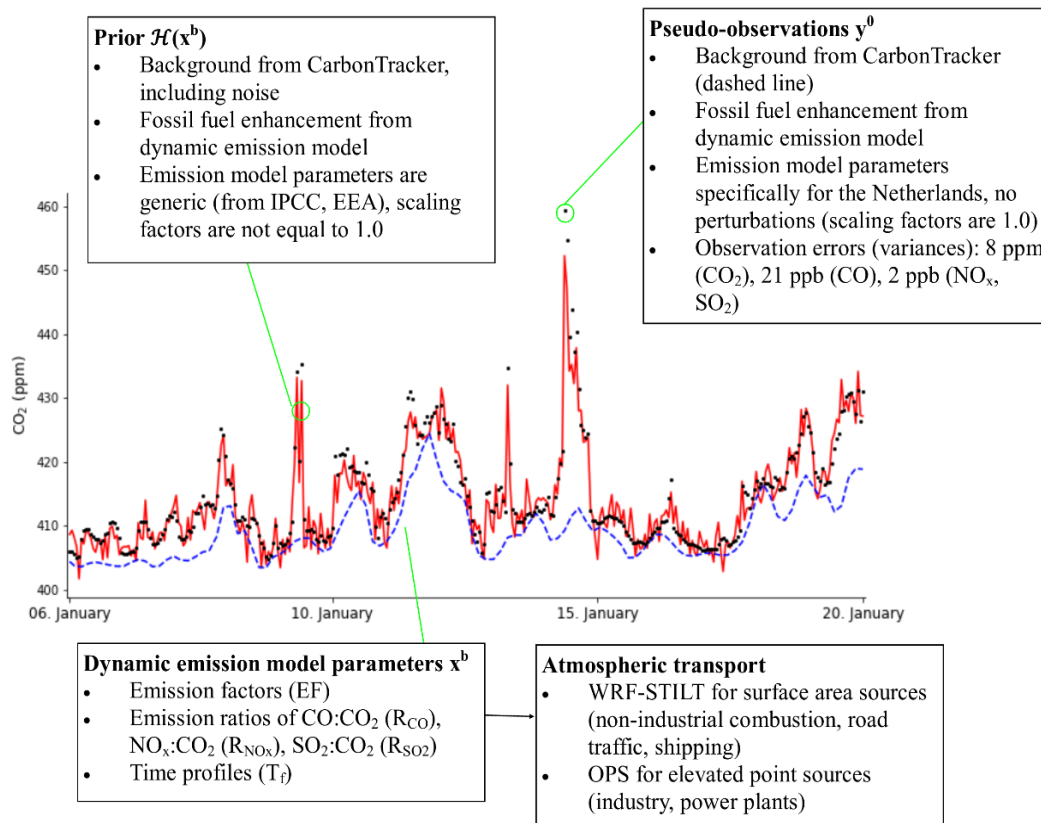
Figure 7. Time series of pseudo-observations and prior CO₂ mole fractions and a summary of how these time series were created.

We have adapted CTDAS for smaller scale studies by replacing the typical observation operator $\mathcal{H}$, which is the global TM5 transport model (Huijnen et al., 2010), with a combination of WRF-STILT footprints and the OPS plume model, building on the methods described in Super et al., (2017a) and He et al. (2018). Moreover, we have added our emission model to the observation operator so that we can sample its parameter distribution in atmospheric mole fraction space. More details about the individual parts of this system are provided below and are summarized in Fig. 7.

2.2.1 Observation operator

The observation operator translates the 44 parameters in the emission model first into emissions (through Eq. (1) and Eq. (2)) and then into atmospheric mole fractions. The transport modelling consists of two parts. The first part, the Weather Research and Forecasting-Stochastic Time-Inverted Lagrangian Transport (WRF-STILT, (Nehrkorn et al., 2010) model, is used for surface emissions that are representative of large areas (i.e., not a point source). STILT is a Lagrangian particle dispersion model that describes the footprint of a single measurement by dispersing particles back in time (Gerbig et al., 2003; Lin et al., 2003). With this footprint the surface influence of emissions on a single observation can be described. An advantage of this method is that it allows the pre-calculation of linear atmospheric transport, which makes this part of the observation operator less computationally demanding than running an ensemble of a full atmospheric transport model (like WRF with chemistry). The total domain covered with WRF-STILT is 77 x 88 km (Fig. 1) and includes most of the Randstad.

The second part of the transport modelling is a plume model. In a previous study we have shown that point source (stack) emissions should be modelled with a plume model to better represent the limited dimensions of the stack

15

432 plume (Super et al., 2017a). Similarly, Vogel et al. (2013) have shown that the surface influence calculated by
433 STILT can lead to large model errors for stack emissions. Therefore, we include the OPS (Operational Priority
434 Substances, short-term version) plume model in our framework to model the transport and dispersion of stack
435 emissions (Van Jaarsveld, 2004; Sauter et al., 2016). OPS provides hourly concentrations at pre-defined receptor
436 points, which represent our measurement sites. We apply the OPS model only to point source emissions within
437 the Rijnmond area, as we found in a previous study that a plume model only has an added value less than 10–15
438 km downwind from the stack (Super et al., 2017a). Point sources at more than 10–15 km from the observation site
439 can be sufficiently represented with a Eulerian model. The OPS model input includes detailed information about
440 the exact stack height and heat content of the plume. For more details on WRF-STILT and OPS see Appendix C.
441 In addition to the fossil fuel contribution we also include background mole fractions for CO_2 and CO. NO_x and
442 SO_2 are short-lived and therefore the variations in the background are relatively small compared to the fossil fuel
443 signals. The CO_2 background is taken from the 3-D mole fractions of CarbonTracker Europe (Peters et al., 2010)
444 and also accounts for biogenic fluxes. The resolution of these CO_2 fields is 1x1° and we select the grid box that is
445 situated over Rotterdam. The 3-hourly data are linearly interpolated to get hourly background mole fractions that
446 are added to the fossil fuel signals calculated by the transport models. We use the strong wintertime correlation
447 between CO_2 and CO mole fractions (r = 0.73) to calculate CO background conditions from the CO_2 background.
448 This is not very accurate, but for the purpose of this OSSE it provides us with a decent estimate of the variability
449 in background mole fractions.

2.2.2 State vector

451 We populated the state vector with a selection of the most important parameters of the emission model, based on
452 their impact on the total emission uncertainty described in the results (Sect. 3.1). However, we hypothesize that
453 emission model parameters that are not part of the state vector are nevertheless uncertain and may affect the results.
454 Therefore, we include a total of 44 scaling factors in our state vector (x^b), and each scaling factor is linearly related
455 to a parameter from the emission model. The uncertainty in these parameters (covariance matrix P) is derived from
456 the Monte Carlo simulations described in Sect. 2.1, with the spread in the emission model parameter values
457 provided by the same databases of the IPCC and EEA. These uncertainty values can also be found in Appendix A.
458 For this study we selected an arbitrary two-week period in January 2014 (6–20 January). Note that during the
459 summer the importance of source sectors might be different, e.g. there will be less heating from households.
460 Nevertheless, this period is sufficient to test the applicability of our DA system. We loop over the 14 days in our
461 study period, resulting in one posterior state vector for each day. We initialize our state vector for every new day
462 using the posterior values and posterior uncertainties from the previous day. Because the footprints we generated
463 extend backwards for six hours, the state vector for each day is effectively only constrained by the observations
464 from that same day, and hence we did not use a Kalman-smoother approach in this work in contrast to other
465 CTDAS applications.
466 Although this is a data-rich region, we use generic values for the prior emission model parameters which we take
467 from the IPCC, EEA and other organisations (Appendix A). These values are typically valid for a large region
468 (e.g. Europe) and not necessarily the best estimate for our regional case study. The reason that we use these values
469 is that they can provide a first estimate of the emissions in data-scarce regions where inverse modelling might add

470   most to our knowledge. With this set-up we can examine how well we can constrain the true emissions starting

471   with this generic, and widely available, information.

472   One major challenge in this study is to attribute the mismatch between the observed and modelled mole fractions

473   to a specific sector, as a CO_2 observation alone provides no details on the origin of the CO_2. Therefore, we include

474   three tracers (CO, NO_x and SO_2) that are co-emitted with CO_2 during fossil fuel combustion in a ratio (referred to

475   as R_{CO}, R_{NOx} and R_{SO2}) that is specific for each source sector (Fig. 2). Their (pseudo-)observations can inform us

476   about the source of the mismatch, but through their emission ratio to CO_2 they also constrain the magnitude of

477   CO_2 emissions in the emission model. The ratios R_{CO}, R_{NOx} and R_{SO2} used for this conversion to CO_2 emissions is

478   not fixed: for each of the co-emitted species we included them in the state vector. This recognizes that emission

479   ratios are highly variable and uncertain but play an important role in source attribution.

480   **2.2.3 Pseudo-observations**

481   In this work we create observing system simulation experiments (OSSEs), which use pseudo-observations instead

482   of true observations. The advantage of using pseudo-observations is that we can accurately examine the abilities

483   of our new approach without having to account yet for (often dominant) atmospheric transport errors. This

484   approach represents an ideal situation with relatively few sources of error compared to a study using real

485   observations, which makes it useful to study the potential of this new system to optimize emission model

486   parameters.

487   The pseudo-observations used to optimize the emission model parameters are created using the same observation

488   operator as described above. The emission model is used to create realistic emissions with a high spatiotemporal

489   resolution. Yet in contrast to the prior, we use specific local (Dutch) values for the emission model parameters.

490   These parameters are considered to be the truth and are therefore not scaled (scaling factors are 1.0). We found

491   that these local parameter values are always within the uncertainty range of the general (prior) values, so that the

492   true solution is part of the distribution explored within the prior. This is confirmed in an experiment with a small

493   model-data mismatch and no noise on the background, which reproduces the true parameters very well (not

494   shown).

495   The resulting emissions are used in combination with the background mole fractions and transport calculated by

496   WRF-STILT and the OPS model to create pseudo-observations at the locations shown in Fig. 1. For the pseudo-

497   observations the original background time series are used, whereas in the inversion random noise is added to the

498   background mole fractions with a standard deviation of 2 ppm for CO_2. We assume no contribution from biogenic

499   CO_2 to the excess CO_2 over the background, which means that any biogenic contribution to CO_2 within our

500   footprint is the same as in the inflow from outside our domain, thus cancelling in the subtraction of the background

501   CO_2. An error in biogenic fluxes is therefore attributed to the fossil fuel emissions, which represents a typical case

502   where biogenic and fossil fuel signals are hard to distinguish from each other and from the background. Biogenic

503   fluxes can be significant, even in urban areas, and therefore add significant uncertainty to the fossil fuel flux

504   estimates (Fischer et al., 2017; Sargent et al., 2018).

505   One simulated time series is illustrated in Fig. 7. The monitoring network consists of seven sites that are scattered

506   over the city of Rotterdam and the port. All sites exist in the national CO_2 or air quality measurement networks,

507   although not all species used in the inversion are observed at all locations. We only use the daytime (12–16 h LT)

508   observations to constrain our emissions, resulting in a total of 1960 observations. This is normally done to favour

17

well-mixed conditions when simulated transport is more reliable, and we want to mimic this limitation. We assume all instruments have an inlet at 10m above ground level. In reality this is lower for several sites, but during the well-mixed daytime conditions the difference is minimal. Representing atmospheric transport around in-city sites can be very challenging and therefore the use of elevated sites or a transport model that can represent transport in complex terrain in more detail is recommended when true observations are used.

The covariance matrix R describes the observation error. It accounts for errors related to instrumentation, but also representativeness errors due to model transport, interpolation, and parameterization used in the emission model. Although in principle such errors can be excluded in an OSSE, we prefer to use realistic estimates of these errors to allow for the random errors that we applied to the prescribed boundary inflow, as well as to account for parameters in the emission model that are not optimized even though they contained uncertainty in the pseudo-data creation. We base the R matrix on the calculated errors in the background and atmospheric transport and variability caused by parameters that are not part of the state vector from the uncertainty analysis, and we end up with variances of 2.5 ppm (CO_2), 8 ppb (CO), 3 ppb (NO_x) and 1 ppb (SO_2).

2.3 Data Assimilation Experiments

We perform various experiments to examine the sensitivity of the system to different set-ups and sources of error. The experiments are discussed here, and the detailed set-up of the inversions is summarized in Table 2. The base run is labelled "Base".

1) State vector definition: We start with a comparison of two different state vectors. For this purpose, we compare the base run with an inversion (Short_state) which only includes the 21 most important parameters as identified in the sensitivity analysis. This test allows us to examine the impact of erroneous, non-optimized emission model parameters on the emission estimates. The results are discussed in Sect. 3.2.

2) Source attribution: Next we compare two monitoring network configurations which differ in the number of tracers used. We perform an inversion with CO_2 as the only tracer (CO_2_only) and one with the full range of tracers (Base) to assess the added value of including co-emitted species for source attribution. These tests address the question whether co-emitted species can be used for source attribution. The results are discussed in Sect. 3.2.

3) Propagation: The third experiment is used to examine the effect of propagation of posterior values and uncertainties on the final emission estimates. We compare the base run to a run that has no propagation (No_propagation and CO_2_only_no_propagation) but instead starts from the same prior mean and uncertainty on each of our 14 days considered. The runs without would allow the parameter values to change over time. The results are discussed in Sect. 3.3.

Table 2. Overview of the inversions: which tracers are included, the length of the state vector and whether posterior values and uncertainties are propagated.

| Inversion name	Tracers	State vector length (per day)	Propagation to the next day
Base	All	44	Yes
Short_state	All	21	Yes
No_propagation	All	44	No
CO_2_only	CO_2	44	Yes
CO_2_only_no_propagation	CO_2	44	No

18

3 Results

Before demonstrating the use of our dynamic emission model in an inverse framework, we demonstrate its application as a simple but versatile method to generate hourly gridded emissions for multiple species with full covariances.

3.1 Dynamic emissions and their uncertainty

The total annual emission of CO_2 for the Netherlands calculated with the dynamic emission model is 180 Tg CO_2 with an uncertainty of 15 % (1-sigma Gaussian based on 500 members of a Monte Carlo simulation). This matches the total of the Dutch national emission inventory for 2014 by design (step 1), but the uncertainty on the latter was estimated with a similar Monte Carlo simulation to be only 1 % for CO_2 in 2004 (Ramírez et al., 2006). This smaller uncertainty is fully due to the use of country-specific emission factors with a much smaller range than we derived from the IEA and IPCC inventories. Spatial disaggregation (step 2) does not affect the uncertainty of the domain aggregated annual fluxes, and the time profiles (step 3) have no impact on the annual total emissions. For CO, NO_x and SO_2 the uncertainties in the emission model are much larger, with medians (CI's) of $6.5x10^8$ ($1.3x10^8$–$6.8x10^9$) kg CO yr^{-1}, $5.0x10^8$ ($1.2x10^8$–$5.1x10^9$) kg NO_x yr^{-1}, and $1.3x10^8$ ($5.1x10^6$–$2.2x10^{10}$) kg SO_2 yr^{-1}. These ranges result from uncertainties in the assumed ratios of their release per unit of CO_2 emitted.

At the sub-annual time scale, time profiles have an impact on the uncertainties as well. The daily emissions of the Netherlands depend on the day and the season (Fig. 8) and range from 0.36 to 0.76 Tg CO_2 day^{-1}. The time series shows a seasonal cycle with lower emissions during the summer. There is a clear weekly cycle with reduced emissions during the weekend. The uncertainty in the total daily emission varies between 8 and 15 %, which is similar to or lower than the uncertainty in the annual total emissions. The explanation for these relatively low uncertainties is that many uncertainties are temporally uncorrelated and their impacts on individual days partially cancel out. Moreover, the largest sectors (coal-fired power plants and industry) already have a large uncertainty and adding more uncertainty through the time profiles has little impact. Nevertheless, the uncertainties introduced through the time profiles cause an uncertainty in daily CO_2 emissions of about 7 %, if the other uncertainties are excluded from the analyses.

19
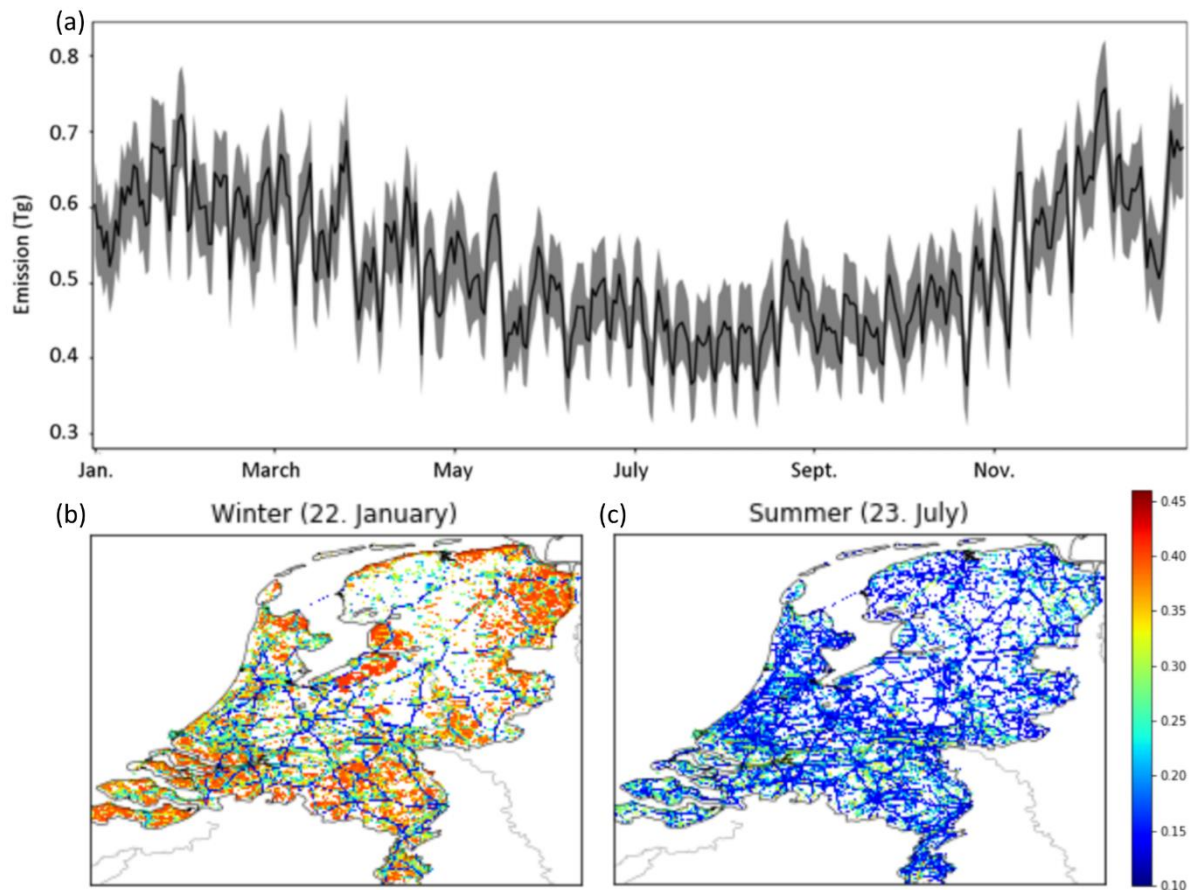
Figure 8. (a) Time series of daily CO_2 emissions (in Tg CO_2 day^{-1}) and their uncertainty. Given is the interquartile range (shaded area) and the median (line) from the ensemble. **(b and c)** Map of annual mean relative uncertainty of emissions for the top 25 % pixels with the largest emissions, during a winter month (dominated by household gas- and electricity use) and a summer month (electricity and road-traffic dominated).

Differences in the relative contribution of different sectors are evident when looking at the map of uncertainties across the Netherlands (Fig. 8), reflecting both the most uncertain parameters, but also the dominant source sectors. Winter emissions for example are dominated by household gas-usage, while industrial and traffic emissions give rise to uncertainty year-round at a 10–30 % level. We further identified the most important parameters per source sector with a Monte Carlo simulation per source sector (Fig. 9). Results shows that the road traffic and shipping sectors contain the smallest relative uncertainties, although the time profile for shipping causes an uncertainty of about 7 % in the total shipping emissions. The industrial emissions are most uncertain, and this is almost exclusively due to the emission factor, which causes an uncertainty of 41 % in the total industrial emissions. Similarly, the power plant emissions have a large relative uncertainty due to the uncertain emission factor of coal-fired power plants (19 %). Also, for households and glasshouses the emission factor is uncertain (14 % and 26 %, respectively), but here the time profiles also have a large impact (10 % and 16 %, respectively).

20
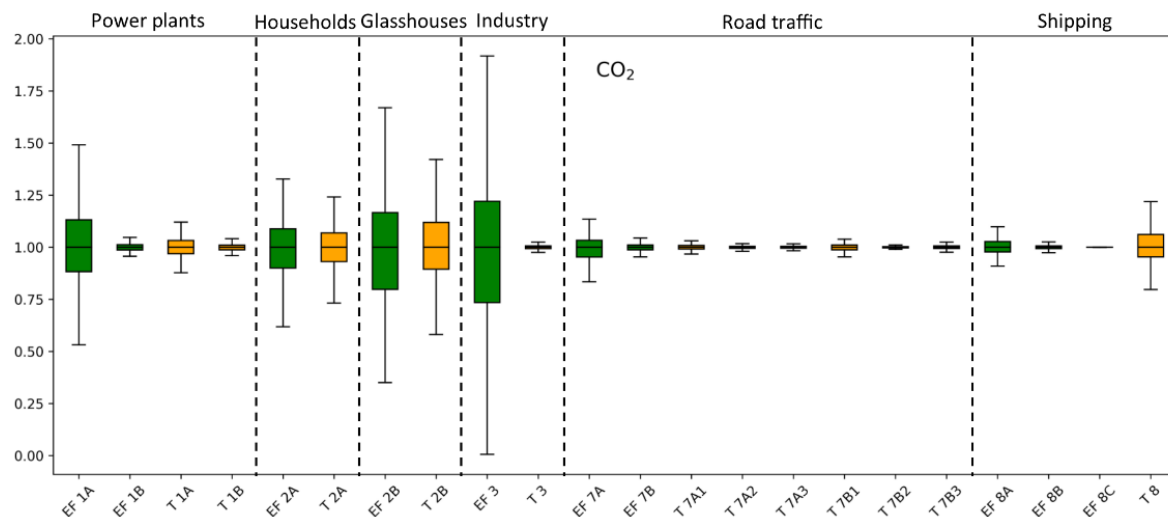
Figure 9. Box plots showing the uncertainty in the CO_2 emissions from power plants (1A+1B), households (2A), glasshouses (2B), industry (3), road traffic (7A+7B) and shipping (8A+8B+8C) caused by individual parameters affecting that sector. Uncertainty is represented as the spread in daily (normalized) emissions from each ensemble member (N=500) for a randomly chosen day. EF refers to an emission factor (green bars) and T to a time profile (orange bars). (Sub)sectors are indicated with their short names as summarized in Table 1. Note that the time profiles of road traffic emissions are specified per road type (1 = highway, 2 = main road, 3 = urban road). Minor parameters that have very small impacts on CO_2 emissions are not shown here (23 out of 44).

3.2 Optimizing dynamic emissions

In the base inverse modelling setup, our system is able to improve the mean estimate and reduce the uncertainty on total CO_2, CO, NO_x, and SO_2 emissions. Figure 10 shows the probability density function of these estimated total emissions, compared to the prior (using parameters derived from IPCC/EEA) and the truth (created with country-specific parameter values). Interestingly, the posterior result deteriorates slightly when using a shortened state vector in which 11 parameters of "minor" influence (such as the SO2:CO_2 ratio of household emissions) are not optimized from their incorrect prior. This is caused by sporadic atmospheric signals that are dominated by household emissions, even if these emissions only contribute a small fraction to the total emissions. These signals are then used to update the emission factor, while the emission ratios are also incorrect.

21
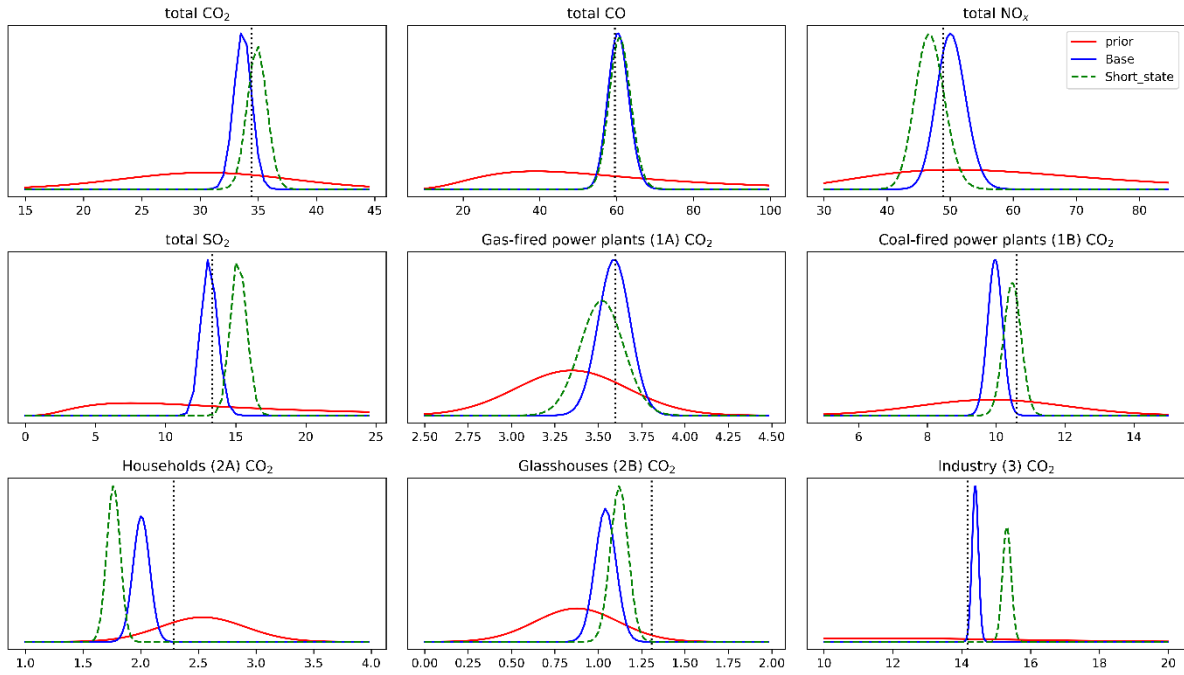
Figure 10. Probability density functions of emissions per species or per source category (for CO₂) in units of Tg (CO₂) or Gg (CO, NOx, SO2). The truth is shown as a vertical dotted line, typically well-matched by the mean of the posterior in blue. Using a shortened state vector (green dashed line) deteriorates the total non-CO₂ emissions substantially and leads to misattribution of CO₂ emissions in minor categories such as 2A (households).

With CO_2 as the only tracer in the inversion we find that we can still estimate total CO_2 emissions (truth-minus-optimized = 0.03 Tg CO_2 yr^{-1}), but we lose the capacity to attribute emissions to specific sectors. Instead, mainly the emission factor of the largest single source being industry (EF3) is optimized. We illustrate this in Fig. 11, using the No_propagation run. The large spread across the 14 individual days indicates that the emission factor jumps around within a large prior uncertainty distribution and is not well-constrained on each day. Some of the other emission factors show almost no deviation from the prior and little variability. Given the constraints posed by CO_2 observations alone, and the limited number of parameters that change the simulated CO_2, optimizing EF3 improves the results at the lowest costs. Introducing the co-emitted species allows the system to identify the source of a residual, and attribute it to the right parameters if sufficient sensitivity is present. This is especially true for those sectors that have relatively small emissions and/or uncertainties, like 2B and 1A. This is corroborated by the posterior covariance matrices (See Appendix D) which show a reduction in parameter correlations for those parameters (i.e., a better mathematical separation of the estimates) when all tracers are included in the estimate. For other parameters the median values are further from the truth than the prior (e.g. for R_{SO2} 8), which indicates that there is too little sensitivity to these parameters.

22

619
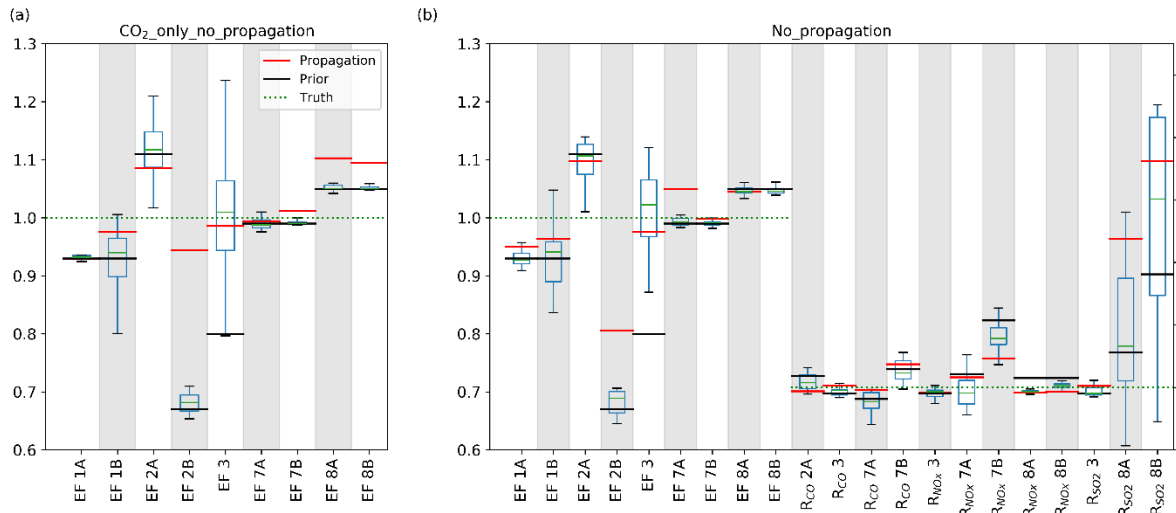
Figure 11. Spread (Q1-Q3) and median values of the parameter scaling factors for the fourteen individual days included in the CO₂_only_no_propagation (a) and No_propagation (b) inversions, and final value of the CO₂_only (left) and base (right) inversion (red lines). The prior values are indicated by the black lines and the truth is indicated with the green dotted lines (value of 1.0). The left y-axis is for the emission factors, the right y-axis for the tracer ratios. The inversion with all tracers shows more variability in the emission factors and larger deviations from the prior values.

3.3 Localization and propagation of information

Propagating information on parameter values from one day to the next is often better than using the median of individual days' estimates as illustrated by the red lines in Fig. 11. Nevertheless, the sporadic detection of plumes with specific signatures suggests that a form of selection or localization of the strongest signals could reduce noise and improve the estimate for the No_propagation run. We therefore ranked the 14 daily independent parameter estimates based on their relative posterior uncertainty and the residuals in an attempt to find the most trustworthy parameter values. This ranking is done per parameter, so the best estimate of different parameters can be related to different days. The increase in residual (same for all parameters) and posterior uncertainty (of the industrial emission factor) is shown in Fig. 12, where the 3–5 highest ranked days have similar characteristics after which the reliability decreases. On the lower ranked days, atmospheric signals from that particular source sector are too small (or even absent) to update the parameters related to that source sector. A similar pattern is found for the other parameters (not shown), with 2–5 days of high sensitivity out of 14.

637
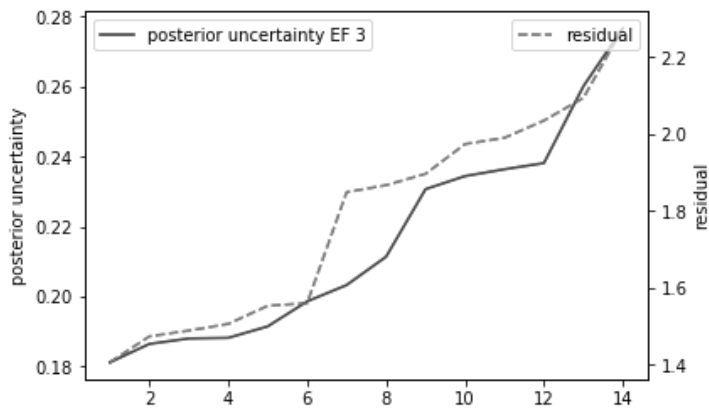
Figure 12. Increase in posterior uncertainty (1σ of unitless scaling factor) in the industrial emission factor (EF 3) and absolute mean residual of CO₂ (in ppm) from highest- to lowest-ranked days.

640

23

641   When we use the top-3 averaged parameter values to calculate emissions we find for most sectors that the emission

642   estimate is similar to the base run, albeit with a larger uncertainty, while for a few specific sectors results

643   deteriorate. This suggests that selecting for strong signals can dampen spurious noise, but still does not improve

644   on the base run that includes full propagation of the covariances, hence carrying information on parameter

645   correlations that is partially lost in the No_propagation run.

646   From the posterior covariance matrices we can confirm our selection of "good" days, as these typically show

647   relatively weak correlations between parameters. For the industrial sector (emission factor, R_{NOx}, R_{SO2}) these are

648   typically weak on most days, and indeed the mean over the entire period already gives a robust estimate of the true

649   parameter value (Fig. 13). The parameters with the strongest correlations are R_{CO} of households and road traffic,

650   and their mean values tend to be dominated by a few outliers. Selecting days on which the posterior parameter

651   correlations are weak (i.e. the atmospheric signal clearly contains information about this specific parameter) results

652   in a large improvement compared to the prior or a 14-day average. Moreover, these results show a similar or better

653   performance as the top-3 selection based on Fig. 12 (0.08 for EF3 and 0.18 for R_{co} 7A, not shown), and are closer

654   to the base run.
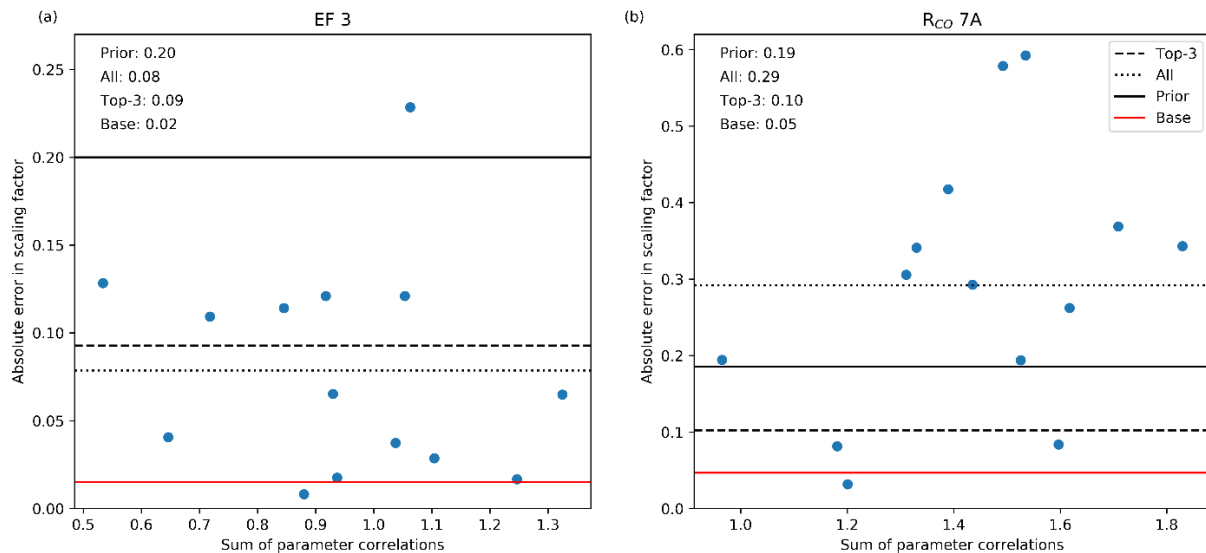
656   **Figure 13. Scatter plot of the absolute error in the scaling factor of the industrial emission factor (EF 3) and R_{CO} of road**
657   **traffic (7A) against the sum of the parameter correlations of the same parameters. The correlation coefficients are -0.17**
658   **and 0.37 respectively. The horizontal lines give the average absolute error in the scaling factor for the prior (full black**
659   **line), if all 14 days are averaged (dotted line), and based on the 3 days with the smallest parameter correlations (dashed**
660   **line) and the result for the base run (full red line). The values are also given.**

661   **4 Discussion**

662   **4.1 Optimizing the dynamic emission model**

663   The dynamic emission model has the advantage over static emission fields that its parameters are optimized, giving

664   more detailed physical meaning to the results. To reduce the size of the problem, the state vector can be populated

665   with those parameters that are most important and/or uncertain. However, we find that other uncertain parameters

666   that are not part of the state vector can still significantly affect the optimization. Therefore, the size of the state

667   vector should be considered carefully when applying this method. How to best determine the size of the state

668   vector requires further work, possibly using some objective criterion to select for a dynamic model with an optimal

669   information content (Akaike, 1974). Moreover, we performed an experiment to establish the possibility to optimize

24

the time profiles as part of the state vector. Although we found small improvements for some sectors, it appears to be difficult to differentiate between the different variables in Eq. (2) that have a linear relationship based purely on the observations. Therefore, the results are not shown and optimizing the temporal dynamics of the emission model requires further work. In a future study the uncertainty caused by spatial disaggregation should also be included, as well as the possibility to reduce this uncertainty using higher-resolution satellite observations (Kuhlmann et al., 2019).

Additionally, we identified the base run as the simplest method to get good estimates, but we do note that our current propagation scheme does not yet include error growth. That means that eventually the ensemble will converge on a parameter value and discard incoming observational evidence, unless the covariance is inflated to allow new updates. Examples of such a covariance inflation scheme are ample in literature and in principle not difficult to include, but were not yet considered in this work as the time periods covered were still short. An example related to this work is to use weather system characteristics to determine a correlation length for household emissions.

Finally, we have demonstrated that tracers are suitable for source attribution. Several previous studies have used co-emitted species as tracer for fossil fuel CO_2 by taking advantage of the specific emission ratio characteristics of each source sector (Lauvaux et al., 2013; Lindenmaier et al., 2014; Turnbull et al., 2015) and came to similar conclusions. Nevertheless, the uncertainty in emission ratios remains a source of error and therefore the optimization of emission ratios with our system is a promising step forward. Using co-emitted species to identify the total fossil fuel contribution to the observed CO_2 signal is more difficult (Turnbull et al., 2006). The reason for this is that there is a large variability in emission ratios between sectors. This makes it difficult to establish an average emission ratio for an urban area, because it depends strongly on the relative contribution of each source sector and may vary over time.

4.2 Radiocarbon and background definition

Therefore, a nice addition to this inversion system would be the inclusion of radiocarbon measurements. The radiocarbon isotope ($^{14}CO_2$) can be used to simulate fossil fuel CO_2 records and has been applied successfully in several inverse modelling studies (Turnbull et al., 2006; Levin and Karstens, 2007; Miller et al., 2012; Turnbull et al., 2015; Basu et al., 2016; Wang et al., 2018). The radiocarbon measurements could be used directly in the inversion (as we did with the co-emitted species) or be used to define a fossil fuel CO_2 record in advance (Fischer et al., 2017; Graven et al., 2018). Our urban network detects average fossil fuel CO_2 signals of about 5 ppm with peaks up to 50 ppm. This would result in $\Delta^{14}C$ signals (the ratio of $^{14}CO_2$ to $^{12}CO_2$) of around 13 up to 130 per mille, which are certainly detectable with current techniques. However, observations of carbon isotopes are expensive and currently not widely available, so their applicability is still limited. Besides $\Delta^{14}C$ other isotope signatures and tracers can also provide additional information. For example, $^{13}CO_2$ and O_2/N_2 can give insight in the dominant sources and sinks or fuel types (Lopez et al., 2013; Van der Laan et al., 2014) and as such be an indicator for the transition from fossil fuels to biofuels. They might also help to separate between the stack emissions of industry and coal- and gas-fired power plants.

An additional advantage of including the radiocarbon isotope is that the uncertainty in the background CO_2 can be excluded, i.e. only the fossil fuel record is considered. Here, we choose to ignore the uncertainty in the background, except in the definition of the covariance matrix R, and attribute all tracer residuals to the fossil fuel emissions.

25

709   Yet an incorrect definition of the background causes a large bias in the optimized emissions (Göckede et al., 2010).
710   There are also several other methods to deal with the non-fossil fuel related CO_2 signals. First, the uncertain
711   background can be added to the state vector and be optimized in the inversion. For example, He et al. (2018) have
712   shown that high-altitude aircraft observations are suitable to improve regional biosphere flux estimates by
713   correcting the bias in boundary conditions. Second, a mole fraction gradient over the area of interest can be
714   calculated using an upwind and downwind site such that the boundary inflow plays no role anymore (Turnbull et
715   al., 2015). This method was shown to reduce the impact of boundary inflow, but only when the wind direction is
716   more or less perpendicular to the gradient (Bréon et al., 2015; Staufer et al., 2016). Therefore, this method limits
717   the amount of useful measurements.

718   **4.3 Error correlations**

719   The emission model also allows us to study the correlations between model parameters, therefore giving more
720   insight in how information can be used in the system and which parameters are more challenging to separate.
721   Previously, Boschetti et al. (2018) have used the presence of error correlations between emissions of different
722   species and found that this reduces the posterior uncertainties for all species. They even show that the uncertainty
723   reduction increases with the correlation and that an incorrect definition of the error correlations may cause a
724   systematic bias in the posterior emission estimate. However, error correlations are only beneficial if the
725   atmospheric observations can distinguish between the correlated parameters. If this is not the case the presence of
726   parameter correlations can result in poorly constrained parameters and/or large posterior uncertainties. This is
727   especially true when parameters are sensitive to parameter correlations, as we show for R_{CO} of road traffic.
728   An important question is then why some emission model parameters are more sensitive to the presence of
729   parameter correlations than others. One hypothesis is that parameters with a lower prior uncertainty are more
730   sensitive to the presence of parameter correlations. The idea behind this is that if we reduce the diagonal value
731   (uncertainty) by a factor of 4 the off-diagonal value (parameter correlation) reduces by a factor of 2. This means
732   that the parameter correlation is relatively stronger if the uncertainty is lower (Boschetti et al., 2018). This
733   hypothesis cannot be confirmed by our results, as we only find a correlation of -0.27 between the prior uncertainty
734   and the sensitivity to parameter correlations (defined as the correlation between the posterior uncertainty and the
735   sum of the parameter correlations). The main difficulty here is that not all parameters can be discerned with the
736   observed atmospheric signals. Although we included the additional co-emitted tracers for source attribution, the
737   emission ratios have a large uncertainty and the system can have difficulties assigning residuals to either the
738   emission ratio or the emission factor. Yet if we calculate an average sensitivity and total posterior uncertainty per
739   sector (by combining the emission factor and emission ratios per sector) we find a correlation coefficient of -0.82.
740   This suggests that this hypothesis might indeed be correct and source sectors with larger parameter uncertainties
741   are less sensitive to the presence of parameter correlations.

742   **4.4 Atmospheric transport model errors**

743   In addition to the experiments described in Sect. 2.3 we conducted an experiment that focused on the role of
744   transport model errors by using observed meteorology to drive the OPS model in the inversion. Like many authors
745   before us (McKain et al., 2012; Brioude et al., 2013; Lauvaux et al., 2013; Bréon et al., 2015; Boon et al., 2016)
746   we found a large impact on the performance of our system and once again confirmed the need for accurate transport

26

models. This experiment is not further shown in this work because of its redundancy with previous conclusions. Nevertheless, we performed this experiment to examine whether transport errors are important when the state vector consists of parameters that are valid for the entire domain. Random errors, such as errors in the wind direction, are unlikely to affect the optimized emissions much when averaged over a longer time period and domain. This was shown by Deng et al. (2017), who found little variation in the average CO_2 emission for Indianapolis using different configurations of WRF to calculate the transport. However, they did find an impact on the spatial distribution of the emissions. This becomes important when optimizing a specific source sector that is clustered in one place, such as the glasshouses. We found that the glasshouse sector is only correctly optimized with a specific wind direction. If the modelled wind direction is wrong the residuals would thus not be attributed to the glasshouse sector as it is not in the modelled footprint of the measurement site. As such, we conclude that the footprint definition has an impact on the optimized parameters, despite that the parameters have no spatial distribution. Similarly, Broquet et al. (2018) mention that the location and structure of a simulated urban plume might differ significantly from the true plume characteristics due to errors in the simulated wind speed and wind direction.

Systematic errors, whether in the modelled transport or in the observations, are more difficult to solve as they do not cancel out when simulating a longer period, and this can lead to biased emission estimates (Meirink et al., 2008; Su et al., 2011). Several methods have been suggested to overcome problems with an incorrect description of atmospheric transport, such as using an ensemble of atmospheric transport model simulations (Angevine et al., 2014) or the assimilation of meteorological observations (Lauvaux et al., 2013). The latter showed lower biases in buoyancy and mean horizontal wind speed. Another method that is often used is the selection of well-mixed afternoon hours to exclude stable conditions under which pollutant dispersion is often poorly represented (Lauvaux et al., 2013; Bréon et al., 2015; Boon et al., 2016). Such data selection however leads to a bias in the estimated emissions when the diurnal cycle is not correctly accounted for (Super et al., 2020).

Here, we also applied a daytime selection criterion to mimic this situation. However, we found that night time hours could be very useful to constrain our emissions. In our DA system we use residual fossil fuel enhancements over a background (prior - true mole fraction enhancement) to constrain the fossil fuel fluxes. The larger the residual, the more information can be gained from it since the impact of the observation error (R matrix) is relatively small. If, for example, the industrial emission factor is underestimated by 10 %, the residual industrial enhancement (given a linear relationship between the emission factor and the total emission from this sector) will be 10 % of the pseudo-observed mole fraction. This means that a large signal from the industry is needed to reach a residual that is larger than the observation error (σ is 1.6 ppm for CO_2). Looking at the time series of pseudo-observations we find that such large signals mostly occur during night time or in the early morning. Therefore, the inversion could benefit strongly from an improved description of night time boundary layers and stable conditions, so that the large night time enhancements can be used to constrain the fossil fuel fluxes.

5 Conclusions

The aim of this study was to examine how well our DA system can quantify urban CO_2 emissions per source sector. Since the prior consists of a dynamic fossil fuel emission model the model parameters are optimized rather than the emissions themselves. The parameters are related to specific source sectors and to attribute residuals to these sectors measurements of additional tracers (CO, NO_x and SO_2) are included in the inversions. We tested this

27

system to examine its ability to overcome some major limitations in current urban-scale inversions: source attribution, definition of the prior and its uncertainties, and the sensitivity to errors in atmospheric transport.

We find that inverse modelling at the urban scale is feasible when the observations contain a lot of information about the different source sectors. Based on this work we can conclude:

1. A dynamic fossil fuel emission model can be useful to create a prior in data-sparse regions or to make use of local data to increase the spatiotemporal representation, while allowing to constrain physically relevant parameters in more detail.

2. When only CO_2 mole fractions are used in the inversion the total CO_2 emissions are well-constrained, but additional tracers are an important addition to the inversion framework in order to discern the information belonging to specific source sectors and emission model parameters. However, even more tracers might be needed to fully capture the heterogeneity of the emission landscape.

3. The prior error covariance structure based on the emission model provides useful insight in how parameters interact and what is needed to separate them.

Nevertheless, several challenges remain. Transport modelling at this small scale needs to be improved to be able to use real urban observations, as under current conditions the transport error strongly dominates the results. Especially improving the description of night time boundary layers could be beneficial, because large atmospheric signals mostly occur during this period. For the future, additional advances need to be made to include satellite observations in the inverse modelling framework. The advantage of satellite data is that it covers data-sparse regions and with a larger view it can differentiate between the urban dome with high pollution levels and the cleaner rural areas, which is a nice addition to in situ measurements.

Code and data availability

CTDAS (v1.0) (Van der Laan-Luijkx et al., 2017) is released under a GNU-GPL3.0 license and forms the basis of the system described in this paper. Minor changes have been made to include the dynamic emission model. Revised code and the additional module used to describe the dynamic emission model and the creation of pseudo-observations is included as Supplement, as is a script used for the emission uncertainty analysis (Monte Carlo simulation). Input data for the dynamic emission model are taken from open, online databases and are summarized in Appendix A, including their data sources. Example input files for CTDAS and the OPS model are also included as Supplement.

28

Appendix A: Emission model input data and uncertainties

815   **Table A1. Overview of all parameters in the dynamic emission model, their unit, function type, expected value and**
816   **uncertainty (range).**

Parameter	(Sub)sector	Unit	Function type	Expected value	Uncertainty
Emission factor[a]	Coal-fired power plants[c]	kg PJ^{-1}	Normal	1.01E8	23 %
	Gas-fired power plants[c]	kg PJ^{-1}	normal	5.61E7	10 %
	Households[c]	kg PJ^{-1}	normal	5.89E7	14 %
	Glasshouses[c]	kg PJ^{-1}	normal	5.61E7	25 %
	Industry[d]	kg PJ^{-1}	normal	7.66E7	40 %
	Road traffic cars[e]	kg PJ^{-1}	normal	7.24E7	10 %
	Road traffic HDV[e]	kg PJ^{-1}	normal	7.33E7	5 %
	Ocean shipping[f]	kg PJ^{-1}	normal	7.76E7	5 %
	Inland shipping[f]	kg PJ^{-1}	normal	7.30E7	5 %
	Recreational shipping[f]	kg PJ^{-1}	normal	7.10E7	5 %
Emission ratio CO:CO$_2$	Coal-fired power plants[e]	kg kg^{-1}	lognormal	1.29E-4	8.7E-7–2.9E-4
	Gas-fired power plants[e]	kg kg^{-1}	lognormal	8.47E-4	3.4E-4–2.5E-3
	Households[e]	kg kg^{-1}	lognormal	3.88E-3	8.3E-4–9.6E-3
	Glasshouses[e]	kg kg^{-1}	lognormal	5.40E-4	3.1E-5–7.7E-4
	Industry[d]	kg kg^{-1}	normal	2.06E-3	40 %
	Road traffic cars[e]	kg kg^{-1}	lognormal	1.32E-2	8.0E-5–6.5E-2
	Road traffic HDV[e]	kg kg^{-1}	lognormal	2.22E-3	9.3E-5–1.3E-2
	Ocean shipping[f]	kg kg^{-1}	normal	2.32E-3	30 %
	Inland shipping[f]	kg kg^{-1}	normal	3.42E-3	30 %
	Recreational shipping[f]	kg kg^{-1}	normal	2.96E-1	30 %
Emission ratio NO$_x$:CO$_2$	Coal-fired power plants[e]	kg kg^{-1}	lognormal	5.94E-4	3.0E-4–9.4E-4
	Gas-fired power plants[e]	kg kg^{-1}	lognormal	2.00E-3	2.6E-4–3.7E-3
	Households[e]	kg kg^{-1}	lognormal	1.50E-3	4.8E-4–3.3E-3
	Glasshouses[e]	kg kg^{-1}	lognormal	1.63E-3	5.0E-4–3.5E-3
	Industry[d]	kg kg^{-1}	normal	6.56E-4	40 %
	Road traffic cars[e]	kg kg^{-1}	lognormal	1.76E-3	9.0E-5–7.5E-3
	Road traffic HDV[e]	kg kg^{-1}	lognormal	1.11E-2	3.3E-4–3.7E-2

	Ocean shipping[f]	kg kg^{-1}	normal	2.32E-2	30 %
	Inland shipping[f]	kg kg^{-1}	normal	1.37E-2	30 %
	Recreational shipping[f]	kg kg^{-1}	normal	1.97E-3	30 %
Emission ratio SO$_2$:CO$_2$	Coal-fired power plants[e]	kg kg^{-1}	lognormal	1.66E-4	2.9E-5–4.4E-4
	Gas-fired power plants[e]	kg kg^{-1}	lognormal	5.01E-6	2.9E-6–7.2E-6
	Households[e]	kg kg^{-1}	lognormal	2.21E-5	1.4E-5–6.7E-5
	Glasshouses[e]	kg kg^{-1}	lognormal	8.91E-6	5.2E-6–1.3E-5
	Industry[d]	kg kg^{-1}	normal	4.28E-4	40 %
	Road traffic cars[g]	kg kg^{-1}	normal	1.01E-6	100 %
	Road traffic HDV[g]	kg kg^{-1}	normal	8.16E-7	100 %
	Ocean shipping[f]	kg kg^{-1}	lognormal	6.18E-3	3.3E-4–2.0E-2
	Inland shipping[f]	kg kg^{-1}	lognormal	6.57E-3	3.5E-4–3.0E-2
	Recreational shipping[f]	kg kg^{-1}	lognormal	3.14E-4	1.1E-4–7.0E-4
Hourly time factor[h]	Coal-fired power plants	-	normal	1	28 %
	Gas-fired power plants	-	normal	1	43 %
	Industry	-	normal	1	5 %
	Households	-	normal	1	43 %
	Glasshouses	-	normal	1	74 %
	Road traffic cars highway	-	normal	1	18 %
	Road traffic cars main road	-	normal	1	18 %
	Road traffic cars urban road	-	normal	1	18 %
	Road traffic HDV highway	-	normal	1	41 %
	Road traffic HDV main road	-	normal	1	18 %
	Road traffic HDV urban road	-	normal	1	48 %
	Total shipping	-	normal	1	31 %
Energy consumption per activity data[i]	Total power plants	PJ/mln €	-	8.22E-4	-
	Households	PJ/dd[b]	-	0.199	-
	Glasshouses	PJ/dd[b]	-	0.061	-
	Industry	PJ/mln €	-	7.05E-4	-
	Road traffic cars	PJ/mln €	-	3.98E-4	-

	Road traffic HDV	PJ/mln €	-	2.01E-4	-
	Total shipping	PJ/mln €	-	1.51E-4	-
Fraction of total energy consumption per subsector[j]	Total power plants: coal	-	-	0.62	-
	Total power plants: gas	-	-	0.38	-
	Road traffic cars: highway	-	-	0.47	-
	Road traffic cars: main road	-	-	0.28	-
	Road traffic cars: urban road	-	-	0.25	-
	Road traffic HDV: highway	-	-	0.56	-
	Road traffic HDV: main road	-	-	0.24	-
	Road traffic HDV: urban road	-	-	0.20	-
	Total shipping: ocean	-	-	0.79	-
	Total shipping: inland	-	-	0.20	-
	Total shipping: recreational	-	-	0.01	-

817 [a] Emission factor for coal-fired and gas-fired power plants include uncertainty due to variations in fuel type, including burning

818 of biomass (5 % uncertainty). For households assume 8 % wood combustion based on CO_2 emission values (*Vernieuwd*

819 *emissiemodel houtkachels*, by B.I. Jansen (TNO, 2016)), the remainder is natural gas (with 10 % uncertainty). For glasshouses

820 assume only natural gas combustion, including 20 % additional uncertainty due to use of cogeneration plants. For road traffic

821 cars assume 69 % gasoline, 29 % diesel and 2 % LPG (with 5 % uncertainty); for road traffic HDV assume 100 % diesel.

822 [b] dd = degree day

823 [c] Expected value and uncertainty based on IPCC Emission Factor Database (EFDB) using 2006 IPCC guidelines

824 [d] Expected value based on Netherlands PRTR (emission) and Statistics Netherlands (energy consumption); uncertainty based

825 on expert judgement

826 [e] Expected value and uncertainty based on the EMEP/EEA air pollutant emission inventory guidebook 2016

827 [f] Expected value and uncertainty based on *CO_2, CH_4, and N_2O emissions from transportation-water-borne navigation*, by Paul

828 Jun, Michael Gillenwater, and Wiley Barbour (Good Practice Guidance and Uncertainty Management in National Greenhouse

829 Gas Inventories)

830 [g] Expected value based on Air Pollutant Emission Factor Library (Finish Environment Institute); uncertainty based on expert

831 judgement

832 [h] Uncertainties based on comparison activity data-based time profiles and estimated time profiles from environmental/socio-

833 economic factors (Denier van der Gon et al., 2011)

834 [i] Expected value based on data from Statistics Netherlands (energy consumption, GDP (663008 mln € in 2014)) and Royal

835 Netherlands Meteorological Institute (degree day sum (2313.95 for households, 1443.63 for glasshouses))

836 [j] Expected value based on Netherlands PRTR

837
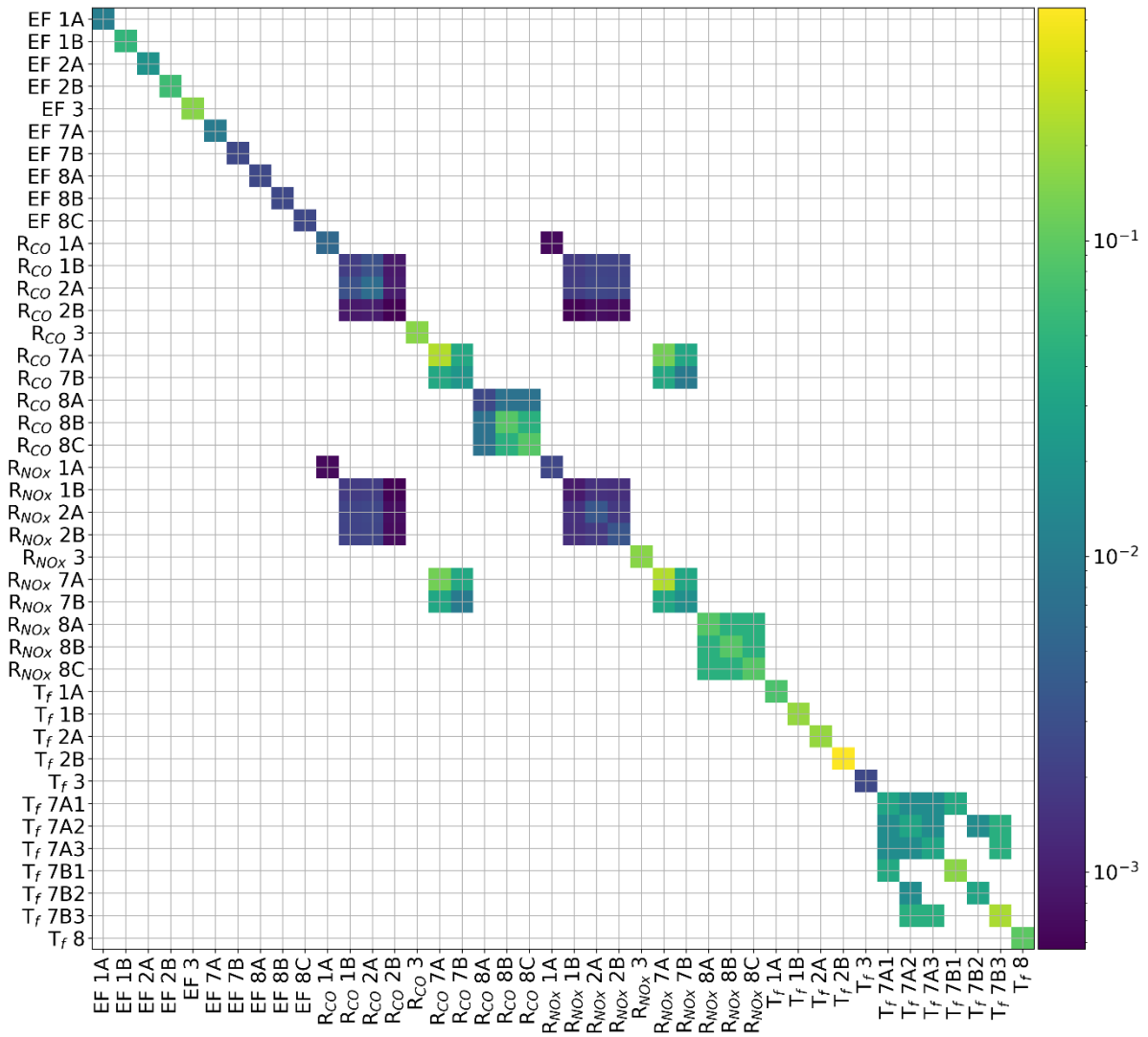
Figure A1. Covariance matrix for all parameters in the emission model. For all covariances we assume a correlation coefficient of 0.5. (Sub)sectors are indicated with their short names as summarized in Table 1. Note that the time profiles of road traffic emissions are specified per road type (1 = highway, 2 = main road, 3 = urban road).

Appendix B: Temporal profiles

Table B1. Overview of the data used to create the temporal profiles presented in Sect. 2.1.2. The activity data represents the actual and the parameterizations are based on environmental variables or other proxies.

Source sector	Subsector	Parameterization	Activity data
Power plants	Gas-fired power plants	Wind speed, solar radiation Threshold: 10 m s^{-1}, 150 J cm^{-2} f: 0.1	Power generation
	Coal-fired power plants	Temperature Threshold: 25°C f: 0.8	Power generation
Non-industrial combustion	Households	Temperature Threshold: 18°C f: 0.2	Gas consumption from smart meters
	Glasshouses	Temperature Threshold: 15°C f: 0	Modelled energy consumption
Industry		None (fixed profile)	
Road traffic	Cars	Average traffic counts	Traffic counts
	Heavy duty vehicles	Average traffic counts	Traffic counts
Shipping	Ocean shipping	None (fixed profile)	
	Inland shipping	Traffic counts	Shipping movements
	Recreational shipping	None (fixed profile)	

The daily time factor of gas combustion for households may be described in terms of two components. First, gas is used for warm water supply and cooking, which is relatively fixed. Second, gas is used for heating, which is strongly temperature dependent. The second component has previously been described using the degree day concept, from which the daily time factor can be defined as:

$$T_t = H/\overline{D} \tag{B1}$$

where H is the heating degree day factor ($H = max(T_{threshold}-\overline{T_{2m}},0)$) based on the daily mean outside temperature at 2 m and a threshold temperature below which heating takes place. $\overline{D}$ is the annual average heating degree day ($\overline{D} = \frac{1}{N}\sum_{j=1}^{N} H$). However, gas consumption related to warm water supply and cooking is largely independent of the outside temperature and therefore a constant offset is included in the heating degree day factor:

$$H_f = H + f \cdot \overline{D} \tag{B2}$$

where f is the constant offset, which is assigned equally to all days The time factor can now be defined as:

$$T_t = H_f/\overline{D_f} \tag{B3}$$

where the average heating degree day accounted for the constant offset $\overline{D_f} = (1 + f)\overline{D}$.

33

858 The Eq. B3 is used for households and coal-fired power plants, whereas for glasshouses no constant offset is
859 assumed and so Eq. B1 is applied. For gas-fired power plants Eq. B3 is used, but the temperature is replaced with
860 average wind speed and solar radiation to match its function as back-up for renewable energy supply:

861 $$H = \max(10 - \bar{u}, 0) \cdot \max(150 - \bar{R}, 0) \qquad (B4)$$

862 where u is the wind speed (m s^{-1}) and R the incoming solar radiation (J cm^{-2} hr^{-1}).

863 **Appendix C: Observation operator**

864 To generate a footprint with the WRF-STILT model, 75 particles are released at the observation site at the start of
865 the back-trajectory and followed back in time. Given that the variability in hourly observations at an urban location
866 is dominated by local signals, we construct back-trajectories spanning 6 hours. This is based on the domain size,
867 which could be covered within 6 hours for typical wind speeds of 4 m s^{-1}. Within this time frame emissions can
868 become well-mixed throughout the boundary layer under normal daytime mixing conditions, such that emissions
869 outside this range can be represented by a boundary inflow. Footprints are generated for each hour within the back-
870 trajectory to account for hourly variations in the emissions. We drive STILT with meteorology from the WRF
871 model (v3.5.1). The WRF model was set up with two nested domains (15x15 and 3x3 km^2 horizontal resolution)
872 and the STILT footprints have a 1x1 km^2 resolution over the entire domain.
873 The OPS plume model keeps track of a plume trajectory, considering time-varying transport over longer distances
874 (e.g. changes in wind direction and dispersion). If for a time step a specific plume affects the receptor, a Gaussian
875 plume formulation is used to calculate the mole fraction caused by that source based on the true travel distance
876 along the trajectory. We drive the model with the same WRF meteorology as STILT. Only primary meteorological
877 variables (temperature, relative humidity, wind direction, wind speed, precipitation, global radiation) are
878 prescribed, secondary variables (e.g. boundary layer height, friction velocity) are calculated by OPS itself and can
879 differ from WRF. Similar to the WRF-STILT model, we assume an influence time of 6 hours on our observations.
880 However, in this case we run the OPS model forward from -6 hours to the time of observation.

881 **Appendix D**
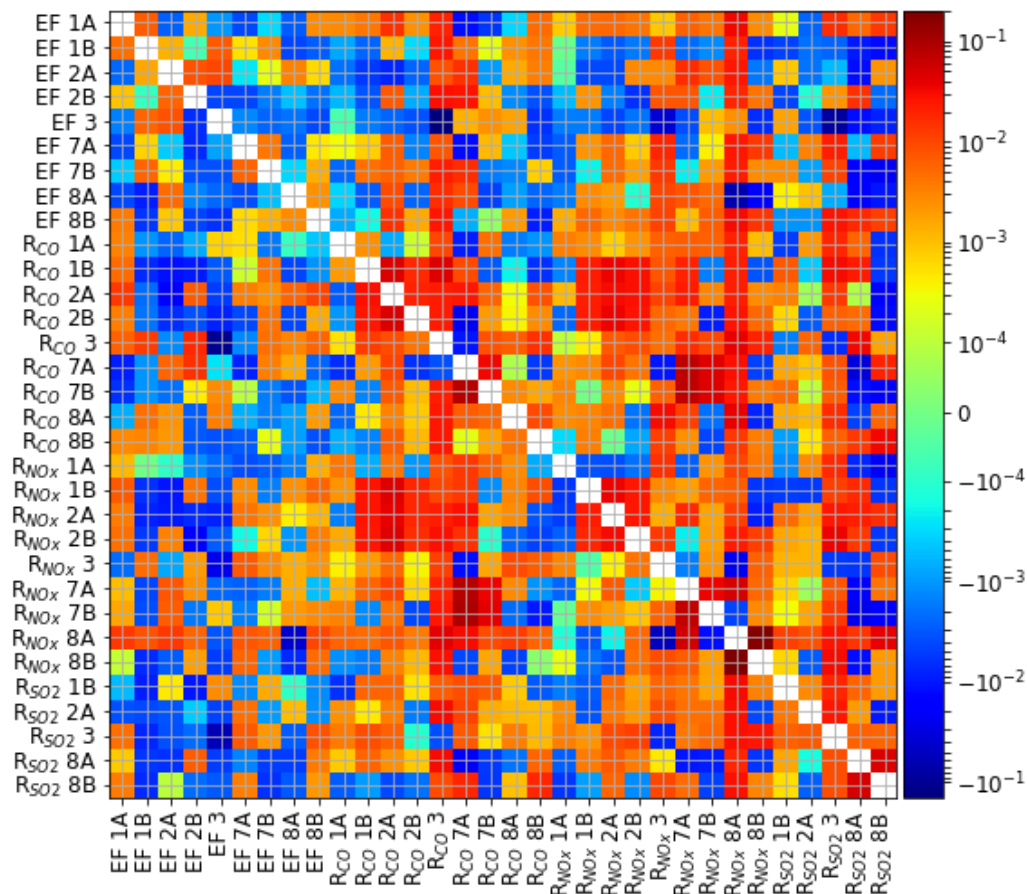
Figure D1. Matrix showing the difference in correlation coefficient (r) between the CO₂_only_no_propagation and No_propagation run averaged for all 14 days, where positive differences indicate reduced parameter correlations when all tracers are included (No_propagation). (Sub)sectors are indicated with their short names as summarized in Table 1. For some parameters a strong reduction in parameter correlations is shown, indicating that with all tracers that parameter can be more easily separated from others, for example the emission factors of industry and coal-fired power plants (EF3 and EF1B).

Author contribution

The initial ideas are developed by WP, IS, HACDvdG and MKvdM. IS and SNCD developed the dynamic emission model. IS and WP are responsible for setting up the inverse modelling experiments and prepared the manuscript with contributions from all co-authors.

Competing interests

The authors declare that they have no conflict of interest.

Acknowledgments

35

900   **References**

901   Akaike, H.: A new look at the statistical model identification, in: Selected papers of Hirotugu Akaike. Springer

902   Series in Statistics (Perspectives in Statistics), edited by: Parzen, E., Tanabe, K., and Kitagawa, G., Springer, New

903   York, NY, 215-222, 10.1007/978-1-4612-1694-0_16, 1974.

904   Andres, R. J., Boden, T. A., and Higdon, D.: A new evaluation of the uncertainty associated with CDIAC estimates

905   of fossil fuel carbon dioxide emission, Tellus B Chem. Phys. Meteorol., 66, 23616, 10.3402/tellusb.v66.23616,

906   2014.

907   Andres, R. J., Boden, T. A., and Higdon, D. M.: Gridded uncertainty in fossil fuel carbon dioxide emission maps,

908   a CDIAC example, Atmos. Chem. Phys., 16, 14979-14995, 10.5194/acp-16-14979-2016, 2016.

909   Angevine, W. M., Brioude, J., McKeen, S., and Holloway, J. S.: Uncertainty in Lagrangian pollutant transport

910   simulations due to meteorological uncertainty from a mesoscale WRF ensemble, Geosci. Model Dev., 7, 2817-

911   2829, 10.5194/gmd-7-2817-2014, 2014.

912   Asefi-Najafabady, S., Rayner, P. J., Gurney, K. R., McRobert, A., Song, Y., Coltin, K., Huang, J., Elvidge, C.,

913   and Baugh, K.: A multiyear, global gridded fossil fuel CO_2 emission data product: Evaluation and analysis of

914   results, J. Geophys. Res.-Atmos., 119, 10,213-210,231, 10.1002/2013jd021296, 2014.

915   Basu, S., Miller, J. B., and Lehman, S.: Separation of biospheric and fossil fuel fluxes of CO_2 by atmospheric

916   inversion of CO_2 and $^{14}CO_2$ measurements: Observation System Simulations, Atmos. Chem. Phys., 16, 5665-5683,

917   10.5194/acp-16-5665-2016, 2016.

918   Boon, A., Broquet, G., Clifford, D. J., Chevallier, F., Butterfield, D. M., Pison, I., Ramonet, M., Paris, J. D., and

919   Ciais, P.: Analysis of the potential of near-ground measurements of CO_2 and CH_4 in London, UK, for the

920   monitoring of city-scale emissions using an atmospheric transport model, Atmos. Chem. Phys., 16, 6735-6756,

921   10.5194/acp-16-6735-2016, 2016.

922   Boschetti, F., Thouret, V., Maenhout, G. J., Totsche, K. U., Marshall, J., and Gerbig, C.: Multi-species inversion

923   and IAGOS airborne data for a better constraint of continental-scale fluxes, Atmos. Chem. Phys., 18, 9225-9241,

924   10.5194/acp-18-9225-2018, 2018.

925   Bréon, F. M., Broquet, G., Puygrenier, V., Chevallier, F., Xueref-Remy, I., Ramonet, M., Dieudonné, E., Lopez,

926   M., Schmidt, M., Perrussel, O., and Ciais, P.: An attempt at estimating Paris area CO_2 emissions from atmospheric

927   concentration measurements, Atmos. Chem. Phys., 15, 1707-1724, 10.5194/acp-15-1707-2015, 2015.

928   Brioude, J., Angevine, W. M., Ahmadov, R., Kim, S. W., Evan, S., McKeen, S. A., Hsie, E. Y., Frost, G. J.,

929   Neuman, J. A., Pollack, I. B., Peischl, J., Ryerson, T. B., Holloway, J., Brown, S. S., Nowak, J. B., Roberts, J. M.,

930   Wofsy, S. C., Santoni, G. W., Oda, T., and Trainer, M.: Top-down estimate of surface flux in the Los Angeles

931   Basin using a mesoscale inverse modeling technique: Assessing anthropogenic emissions of CO, NO_x and CO_2

932   and their impacts, Atmos. Chem. Phys., 13, 3661-3677, 10.5194/acp-13-3661-2013, 2013.

933   Brophy, K., Graven, H., Manning, A. J., White, E., Arnold, T., Fischer, M. L., Jeong, S., Cui, X., and Rigby, M.:

934   Characterizing uncertainties in atmospheric inversions of fossil fuel CO_2 emissions in California, Atmos. Chem.

935   Phys. Discuss., 2018, 1-44, 10.5194/acp-2018-473, 2018.

936   Broquet, G., Bréon, F. M., Renault, E., Buchwitz, M., Reuter, M., Bovensmann, H., Chevallier, F., Wu, L., and

937   Ciais, P.: The potential of satellite spectro-imagery for monitoring CO2 emissions from large cities, Atmos. Meas.

938   Tech., 11, 681-708, 10.5194/amt-11-681-2018, 2018.

939   Chevallier, F., Viovy, N., Reichstein, M., and Ciais, P.: On the assignment of prior errors in Bayesian inversions
940   of CO2 surface fluxes, Geophys. Res. Lett., 33, doi:10.1029/2006GL026496, 2006.

941   Ciais, P., Paris, J. D., Marland, G., Peylin, P., Piao, S. L., Levin, I., Pregger, T., Scholz, Y., Friedrich, R., Rivier,
942   L., Houwelling, S., and Schulze, E. D.: The European carbon balance. Part 1: Fossil fuel emissions, Glob. Change
943   Biol., 16, 1395-1408, 10.1111/j.1365-2486.2009.02098.x, 2010.

944   Deng, A., Lauvaux, T., Davis, K. J., Gaudet, B. J., Miles, N., Richardson, S. J., Wu, K., Sarmiento, D. P., Hardesty,
945   R. M., Bonin, T. A., Brewer, W. A., and Gurney, K. R.: Toward reduced transport errors in a high resolution urban
946   CO_2 inversion system, Elementa (Wash. D.C.), 5, 10.1525/elementa.133, 2017.

947   Denier van der Gon, H. A. C., Hendriks, C., Kuenen, J., Segers, A., and Visschedijk, A.: Description of current
948   temporal emission patterns and sensitivity of predicted AQ for temporal emission patterns, TNO, Utrecht, 2011.

949   Djuricin, S., Pataki, D. E., and Xu, X.: A comparison of tracer methods for quantifying CO_2 sources in an urban
950   region, J. Geophys. Res.-Atmos., 115, 1-13, 10.1029/2009JD012236, 2010.

951   Fauser, P., Sørensen, P. B., Nielsen, M., Winther, M., Plejdrup, M. S., Hoffmann, L., Gyldenkærne, S., Mikkelsen,
952   M. H., Albrektsen, R., Lyck, E., Thomsen, M., Hjelgaard, K., and Nielsen, O.-K.: Monte Carlo (Tier 2) uncertainty
953   analysis of Danish Greenhouse gas emission inventory, Greenhouse Gas Measurement and Management, 1, 145-
954   160, 10.1080/20430779.2011.621949, 2011.

955   Fischer, M. L., Parazoo, N., Brophy, K., Cui, X., Jeong, S., Liu, J., Keeling, R., Taylor, T. E., Gurney, K., Oda,
956   T., and Graven, H.: Simulating estimation of California fossil fuel and biosphere carbon dioxide exchanges
957   combining in situ tower and satellite column observations, J. Geophys. Res.-Atmos., 122, 3653-3671,
958   10.1002/2016jd025617, 2017.

959   Gerbig, C., Lin, J. C., Wofsy, S. C., Daube, B. C., Andrews, A. E., Stephens, B. B., Bakwin, P. S., and Grainger,
960   C. A.: Toward constraining regional-scale fluxes of CO_2 with atmospheric observations over a continent: 2.
961   Analysis of COBRA data using a receptor-oriented framework, J. Geophys. Res.-Atmos., 108,
962   10.1029/2003JD003770, 2003.

963   Göckede, M., Turner, D. P., Michalak, A. M., Vickers, D., and Law, B. E.: Sensitivity of a subregional scale
964   atmospheric inverse CO_2 modeling framework to boundary conditions, J. Geophys. Res.-Atmos., 115,
965   10.1029/2010JD014443, 2010.

966   Graven, H., Fischer, M. L., Lueker, T., Jeong, S., Guilderson, T. P., Keeling, R. F., Bambha, R., Brophy, K.,
967   Callahan, W., Cui, X., Frankenberg, C., Gurney, K. R., LaFranchi, B. W., Lehman, S. J., Michelsen, H., Miller, J.
968   B., Newman, S., Paplawsky, W., Parazoo, N. C., Sloop, C., and Walker, S. J.: Assessing fossil fuel CO_2 emissions
969   in California using atmospheric observations and models, Environ. Res. Lett., 13, 065007, 10.1088/1748-
970   9326/aabd43, 2018.

971   Gurney, K. R., Patarasuk, R., Liang, J., Song, Y., O'Keeffe, D., Rao, P., Whetstone, J. R., Duren, R. M., Eldering,
972   A., and Miller, C.: The Hestia fossil fuel CO2 emissions data product for the Los Angeles Megacity (Hestia-LA),
973   Earth Syst. Sci. Data Discuss., 2019, 1-38, 10.5194/essd-2018-162, 2019.

974   He, W., Van der Velde, I. R., Andrews, A. E., Sweeney, C., Miller, J., Tans, P., Van der Laan-Luijkx, I. T.,
975   Nehrkorn, T., Mountain, M., Ju, W., Peters, W., and Chen, H.: CTDAS-Lagrange v1.0: a high-resolution data
976   assimilation system for regional carbon dioxide observations, Geosci. Model Dev., 11, 3515-3536, 10.5194/gmd-
977   11-3515-2018, 2018.

37

Hirth, L., Mühlenpfordt, J., and Bulkeley, M.: The ENTSO-E Transparency Platform - A review of Europe's most ambitious electricity data platform, Appl. Energy, 225, 1054-1067, 10.1016/j.apenergy.2018.04.048, 2018.

Hogue, S., Marland, E., Andres, R. J., Marland, G., and Woodard, D.: Uncertainty in gridded CO_2 emissions estimates, Earth's Future, 4, 225-239, doi:10.1002/2015EF000343, 2016.

Huijnen, V., Williams, J., van Weele, M., van Noije, T., Krol, M., Dentener, F., Segers, A., Houweling, S., Peters, W., de Laat, J., Boersma, F., Bergamaschi, P., van Velthoven, P., Le Sager, P., Eskes, H., Alkemade, F., Scheele, R., Nédélec, P., and Pätz, H. W.: The global chemistry transport model TM5: description and evaluation of the tropospheric chemistry version 3.0, Geosci. Model Dev., 3, 445-473, 10.5194/gmd-3-445-2010, 2010.

Hutchins, M. G., Colby, J. D., Marland, G., and Marland, E.: A comparison of five high-resolution spatially-explicit, fossil-fuel, carbon dioxide emission inventories for the United States, Mitig. Adapt. Strat. Gl., 22, 947-972, 10.1007/s11027-016-9709-9, 2017.

IEA: World Energy Outlook 2008, International Energy Agency, Paris, 2008.

Kuenen, J. J. P., Visschedijk, A. J. H., Jozwicka, M., and Denier van der Gon, H. A. C.: TNO-MACC-II emission inventory; A multi-year (2003-2009) consistent high-resolution European emission inventory for air quality modelling, Atmos. Chem. Phys., 14, 10963-10976, 10.5194/acp-14-10963-2014, 2014.

Kuhlmann, G. Broquet, G., Marshall, J., Clément, V., Löscher, A., Meijer, Y., and Brunner, D.: Detectability of CO_2 emission plumes of cities and power plants with the Copernicus Anthropogenic CO_2 Monitoring (CO2M) mission, Atmos. Meas. Tech., 12, 6695-6719, 10.5194/amt-12-6695-2019, 2019.

LaFranchi, B. W., Pétron, G., Miller, J. B., Lehman, S. J., Andrews, A. E., Dlugokencky, E. J., Hall, B., Miller, B. R., Montzka, S. A., Neff, W., Novelli, P. C., Sweeney, C., Turnbull, J. C., Wolfe, D. E., Tans, P. P., Gurney, K. R., and Guilderson, T. P.: Constraints on emissions of carbon monoxide, methane, and a suite of hydrocarbons in the Colorado front range using observations of $^{14}CO_2$, Atmos. Chem. Phys., 13, 11101-11120, 10.5194/acp-13-11101-2013, 2013.

Lauvaux, T., Miles, N. L., Richardson, S. J., Deng, A., Stauffer, D. R., Davis, K. J., Jacobson, G., Rella, C., Calonder, G. P., and Decola, P. L.: Urban emissions of CO_2 from Davos, Switzerland: The first real-time monitoring system using an atmospheric inversion technique, J. Appl. Meteorol. Clim., 52, 2654-2668, 10.1175/JAMC-D-13-038.1, 2013.

Lauvaux, T., Miles, N. L., Deng, A., Richardson, S. J., Cambaliza, M. O., Davis, K. J., Gaudet, B., Gurney, K. R., Huang, J., O'Keefe, D., Song, Y., Karion, A., Oda, T., Patarasuk, R., Razlivanov, I., Sarmiento, D., Shepson, P., Sweeney, C., Turnbull, J., and Wu, K.: High-resolution atmospheric inversion of urban CO_2 emissions during the dormant season of the Indianapolis Flux Experiment (INFLUX), J. Geophys. Res.-Atmos., 121, 5213-5236, 10.1002/2015jd024473, 2016.

Levin, I., and Karstens, U.: Inferring high-resolution fossil fuel CO_2 records at continental sites from combined $^{14}CO_2$ and CO observations, Tellus B Chem. Phys. Meteorol., 59, 245-250, 10.1111/j.1600-0889.2006.00244.x, 2007.

Liander: Innovatie & Diensten: Open data: https://www.liander.nl/over-liander/innovatie/open-data/data, last access: Feb 2018.

Lin, J. C., Gerbig, C., Wofsy, S. C., Andrews, A. E., Daube, B. C., Davis, K. J., and Grainger, C. A. C.: A near-field tool for simulating the upstream influence of atmospheric observations: The Stochastic Time-Inverted Lagrangian Transport (STILT) model, J. Geophys. Res.-Atmos., 108, 10.1029/2002jd003161, 2003.

Lindenmaier, R., Dubey, M. K., Henderson, B. G., Butterfield, Z. T., Herman, J. R., Rahn, T., and Lee, S. H.: Multiscale observations of CO_2, $^{13}CO_2$, and pollutants at Four Corners for emission verification and attribution, in: P. Natl. Acad. Sci. USA, 2014, 8386-8391, 2014.

Lopez, M., Schmidt, M., Delmotte, M., Colomb, A., Gros, V., Janssen, C., Lehman, S. J., Mondelain, D., Perrussel, O., Ramonet, M., Xueref-Remy, I., and Bousquet, P.: CO, NO_x and $^{13}CO_2$ as tracers for fossil fuel CO_2: Results from a pilot study in Paris during winter 2010, Atmos. Chem. Phys., 13, 7343-7358, 10.5194/acp-13-7343-2013, 2013.

McKain, K., Wofsy, S. C., Nehrkorn, T., Eluszkiewicz, J., Ehleringer, J. R., and Stephens, B. B.: Assessment of ground-based atmospheric observations for verification of greenhouse gas emissions from an urban region, in: P. Natl. Acad. Sci. USA, 2012, 8423-8428, 2012.

Meirink, J. F., Bergamaschi, P., Frankenberg, C., d'Amelio, M. T. S., Dlugokencky, E. J., Gatti, L. V., Houweling, S., Miller, J. B., Röckmann, T., Villani, M. G., and Krol, M. C.: Four-dimensional variational data assimilation for inverse modeling of atmospheric methane emissions: Analysis of SCIAMACHY observations, J. Geophys. Res.-Atmos., 113, 10.1029/2007jd009740, 2008.

Miller, J. B., Lehman, S. J., Montzka, S. A., Sweeney, C., Miller, B. R., Karion, A., Wolak, C., Dlugokencky, E. J., Southon, J., Turnbull, J. C., and Tans, P. P.: Linking emissions of fossil fuel CO_2 and other anthropogenic trace gases using atmospheric $^{14}CO_2$, J. Geophys. Res.-Atmos., 117, 1-23, 10.1029/2011jd017048, 2012.

Monni, S., Syri, S., and Savolainen, I.: Uncertainties in the Finnish greenhouse gas emission inventory, Environ. Sci. Policy, 7, 87-98, https://doi.org/10.1016/j.envsci.2004.01.002, 2004.

Mues, A., Kuenen, J., Hendriks, C., Manders, A., Segers, A., Scholz, Y., Hueglin, C., Builtjes, P., and Schaap, M.: Sensitivity of air pollution simulations with LOTOS-EUROS to the temporal distribution of anthropogenic emissions, Atmos. Chem. Phys., 14, 939-955, 10.5194/acp-14-939-2014, 2014.

Nakicenovic, N., Alcamo, J., Davis, G., De Vries, B., Fenhann, J., Gaffin, S., Gregory, K., Grübler, A., Jung, T. Y., Kram, T., La Rovere, E. L., Michaelis, L., Mori, S., Morita, T., Pepper, W., Pitcher, H., Price, L., Riahi, K., Roehrl, A., Rogner, H.-H., Sankovski, A., Schlesinger, M., Shukla, P., Smith, S., Swart, R., Van Rooijen, S., Victor, N., and Dadi, Z.: IPCC Special Report on Emissions Scenarios, Cambridge University Press, Cambridge, UK, 2000.

Nassar, R., Napier-Linton, L., Gurney, K. R., Andres, R. J., Oda, T., Vogel, F. R., and Deng, F.: Improving the temporal and spatial distribution of CO_2 emissions from global fossil fuel emission data sets, J. Geophys. Res.-Atmos., 118, 917-933, 10.1029/2012jd018196, 2013.

Nathan, B., Lauvaux, T., Turnbull, J., and Gurney, K.: Investigations into the use of multi-species measurements for source apportionment of the Indianapolis fossil fuel CO2 signal, Elementa, 6, 10.1525/elementa.131, 2018.

Nehrkorn, T., Eluszkiewicz, J., Wofsy, S. C., Lin, J. C., Gerbig, C., Longo, M., and Freitas, S.: Coupled weather research and forecasting-stochastic time-inverted lagrangian transport (WRF-STILT) model, Meteorol. Atmos. Phys., 107, 51-64, 10.1007/s00703-010-0068-x, 2010.

Netherlands PRTR: Netherlands Pollutant Release & Transfer Register: http://www.emissieregistratie.nl/, last access: Mar 2018.

Palmer, P. I., O'Doherty, S., Allen, G., Bower, K., Bösch, H., Chipperfield, M. P., Connors, S., Dhomse, S., Feng, L., Finch, D. P., Gallagher, M. W., Gloor, E., Gonzi, S., Harris, N. R. P., Helfter, C., Humpage, N., Kerridge, B., Knappett, D., Jones, R. L., Le Breton, M., Lunt, M. F., Manning, A. J., Matthiesen, S., Muller, J. B. A., Mullinger,

39

N., Nemitz, E., O'Shea, S., Parker, R. J., Percival, C. J., Pitt, J., Riddick, S. N., Rigby, M., Sembhi, H., Siddans, R., Skelton, R. L., Smith, P., Sonderfeld, H., Stanley, K., Stavert, A. R., Wenger, A., White, E., Wilson, C., and Young, D.: A measurement-based verification framework for UK greenhouse gas emissions: an overview of the Greenhouse gAs Uk and Global Emissions (GAUGE) project, Atmos. Chem. Phys., 18, 11753-11777, 10.5194/acp-18-11753-2018, 2018.

Peters, W., Miller, J. B., Whitaker, J., Denning, A. S., Hirsch, A., Krol, M. C., Zupanski, D., Bruhwiler, L., and Tans, P. P.: An ensemble data assimilation system to estimate CO_2 surface fluxes from atmospheric trace gas observations, J. Geophys. Res.-Atmos., 110, 1-18, 10.1029/2005JD006157, 2005.

Peters, W., Krol, M. C., Van der Werf, G. R., Houweling, S., Jones, C. D., Hughes, J., Schaefer, K., Masarie, K. A., Jacobson, A. R., Miller, J. B., Cho, C. H., Ramonet, M., Schmidt, M., Ciattaglia, L., Apadula, F., Heltai, D., Meinhardt, F., Di Sarra, A. G., Piacentino, S., Sferlazzo, D., Aalto, T., Hatakka, J., Ström, J., Haszpra, L., Meijer, H. A. J., Van der Laan, S., Neubert, R. E. M., Jordan, A., Rodó, X., Morguí, J. A., Vermeulen, A. T., Popa, E., Rozanski, K., Zimnoch, M., Manning, A. C., Leuenberger, M., Uglietti, C., Dolman, A. J., Ciais, P., Heimann, M., and Tans, P.: Seven years of recent European net terrestrial carbon dioxide exchange constrained by atmospheric observations, Glob. Change Biol., 16, 1317-1337, 10.1111/j.1365-2486.2009.02078.x, 2010.

Ramírez, A. R., De Keizer, C., and Van der Sluijs, J. P.: Monte Carlo analysis of uncertainties in the Netherlands Greenhouse Gas Emission Inventory for 1990 – 2004, Copernicus Institute for Sustainable Development and Innovation, Utrecht, 2006.

Rao, P., Gurney, K. R., Patarasuk, R., Song, Y., Miller, C. E., Duren, R. M., and Eldering, A.: Spatio-temporal Variations in on-road CO2 Emissions in the Los Angeles Megacity, AIMS Geosciences, 3, 239-267, http://dx.doi.org/10.3934/geosci.2017.2.239, 2017.

Raupach, M. R., Marland, G., Ciais, P., Le Quéré, C., Canadell, J. G., Klepper, G., and Field, C. B.: Global and regional drivers of accelerating CO_2 emissions, P. Natl. Acad. Sci. USA, 104, 10288-10293, 10.1073/pnas.0700609104, 2007.

Rayner, P. J., Raupach, M. R., Paget, M., Peylin, P., and Koffi, E.: A new global gridded data set of CO_2 emissions from fossil fuel combustion: Methodology and evaluation, J. Geophys. Res.-Atmos., 115, 10.1029/2009jd013439, 2010.

Sargent, M., Barrera, Y., Nehrkorn, T., Hutyra, L. R., Gately, C. K., Jones, T., McKain, K., Sweeney, C., Hegarty, J., Hardiman, B., Wang, J. A., and Wofsy, S. C.: Anthropogenic and biogenic CO_2 fluxes in the Boston urban region, P. Natl. Acad. Sci. USA, 115, 7491-7496, 10.1073/pnas.1803715115, 2018.

Sauter, F., Van Zanten, M., Van der Swaluw, E., Aben, J., De Leeuw, F., and Van Jaarsveld, H.: The OPS-model. Description of OPS 4.5.0, National Institute for Public Health and the Environment (RIVM) Bilthoven, 2016.

Staufer, J., Broquet, G., Bréon, F. M., Puygrenier, V., Chevallier, F., Xueref-Rémy, I., Dieudonné, E., Lopez, M., Schmidt, M., Ramonet, M., Perrussel, O., Lac, C., Wu, L., and Ciais, P.: The first 1-year-long estimate of the Paris region fossil fuel CO_2 emissions based on atmospheric inversion, Atmos. Chem. Phys., 16, 14703-14726, 10.5194/acp-16-14703-2016, 2016.

Su, H., Yang, Z. L., Niu, G. Y., and Wilson, C. R.: Parameter estimation in ensemble based snow data assimilation: A synthetic study, Adv. Water Resour., 34, 407-416, 10.1016/j.advwatres.2010.12.002, 2011.

Super, I., Dellaert, S.N.C., Visschedijk, A.J.H., and Denier van der Gon, H.A.C.: Uncertainty analysis of a European high-resolution emision inventory of CO_2 and CO to support inverse modelling and network design, Atmos. Chem. Phys., 20, 1795-1816, https://doi.org/10.5194/acp-20-1795-2020, 2020.

Super, I., Denier van der Gon, H. A. C., Van der Molen, M. K., Sterk, H. A. M., Hensen, A., and Peters, W.: A multi-model approach to monitor emissions of CO_2 and CO from an urban–industrial complex, Atmos. Chem. Phys., 17, 13297-13316, 10.5194/acp-17-13297-2017, 2017a.

Super, I., Denier van der Gon, H. A. C., Visschedijk, A. J. H., Moerman, M. M., Chen, H., Van der Molen, M. K., and Peters, W.: Interpreting continuous in-situ observations of carbon dioxide and carbon monoxide in the urban port area of Rotterdam, Atmos. Pollut. Res., 8, 174–187, 10.1016/j.apr.2016.08.008, 2017b.

Terrenoire, E., Bessagnet, B., Rouïl, L., Tognet, F., Pirovano, G., Létinois, L., Beauchamp, M., Colette, A., Thunis, P., Amann, M., and Menut, L.: High-resolution air quality simulation over Europe with the chemistry transport model CHIMERE, Geosci. Model Dev., 8, 21-42, 10.5194/gmd-8-21-2015, 2015.

Tolk, L. F., Meesters, A. G. C. A., Dolman, A. J., and Peters, W.: Modelling representation errors of atmospheric CO_2 mixing ratios at a regional scale, Atmos. Chem. Phys., 8, 6587-6596, 10.5194/acp-8-6587-2008, 2008.

Turnbull, J. C., Miller, J. B., Lehman, S. J., Tans, P. P., Sparks, R. J., and Southon, J.: Comparison of $^{14}CO_2$, CO, and SF_6 as tracers for recently added fossil fuel CO_2 in the atmosphere and implications for biological CO_2 exchange, Geophys. Res. Lett., 33, 1-5, 10.1029/2005GL024213, 2006.

Turnbull, J. C., Sweeney, C., Karion, A., Newberger, T., Lehman, S. J., Tans, P. P., Davis, K. J., Lauvaux, T., Miles, N. L., Richardson, S. J., Cambaliza, M. O., Shepson, P. B., Gurney, K., Patarasuk, R., and Razlivanov, I.: Toward quantification and source sector identification of fossil fuel CO_2 emissions from an urban area: Results from the INFLUX experiment, J. Geophys. Res.-Atmos., 120, 292-312, 10.1002/2014jd022555, 2015.

UNFCCC: Paris Agreement, UNFCCC, 2015.

Van der Laan-Luijkx, I. T., Van der Velde, I. R., Van der Veen, E., Tsuruta, A., Stanislawska, K., Babenhauserheide, A., Zhang, H. F., Liu, Y., He, W., Chen, H., Masarie, K. A., Krol, M. C., and Peters, W.: The CarbonTracker Data Assimilation Shell (CTDAS) v1.0: Implementation and global carbon balance 2001–2015, Geosci. Model Dev., 10, 2785-2800, 10.5194/gmd-10-2785-2017, 2017.

Van der Laan, S., Van der Laan-Luijkx, I. T., Zimmermann, L., Conen, F., and Leuenberger, M.: Net CO_2 surface emissions at Bern, Switzerland inferred from ambient observations of CO_2, $\delta(O_2/N_2)$, and ^{222}Rn using a customized radon tracer inversion, J. Geophys. Res.-Atmos., 119, 1580-1591, 10.1002/2013JD020307, 2014.

Van Jaarsveld, J. A.: The Operational Priority Substances model. Description and validation of OPS-Pro 4.1, National Institute for Public Health and the Environment, Bilthoven, 2004.

Vogel, F. R., Thiruchittampalam, B., Theloke, J., Kretschmer, R., Gerbig, C., Hammer, S., and Levin, I.: Can we evaluate a fine-grained emission model using high-resolution atmospheric transport modelling and regional fossil fuel CO_2 observations?, Tellus B Chem. Phys. Meteorol., 65, 10.3402/tellusb.v65i0.18681, 2013.

Wang, Y., Broquet, G., Ciais, P., Chevallier, F., Vogel, F., Wu, L., Yin, Y., Wang, R., and Tao, S.: Potential of European $^{14}CO2$ observation network to estimate the fossil fuel CO_2 emissions via atmospheric inversions, Atmos. Chem. Phys., 18, 4229-4250, 10.5194/acp-18-4229-2018, 2018.

Whitaker, J. S., and Hamill, T. M.: Ensemble data assimilation without perturbed observations, Mon. Weather Rev., 130, 1913-1924, 10.1175/1520-0493(2002)130<1913:EDAWPO>2.0.CO;2, 2002.

1135   Zhou, Y., and Gurney, K. R.: Spatial relationships of sector-specific fossil fuel CO_2 emissions in the United States,

1136   Global Biogeochem. Cycles, 25, 10.1029/2010gb003822, 2011.

1137

1138